Mechanical Design of a Jumping and Self-Balancing Monopedal Robot

by

Evan Brown

Submitted to the
Department of Mechanical Engineering
In Partial Fulfilment of the Requirements for the Degree of

Bachelor of Science in Mechanical Engineering

at the

Massachusetts Institute of Technology

June 2018

Signature redacted

Signature of Author: _____
Department of Mechanical Engineering
May 22, 2018

Signature redacted

Certified by: _____
Sangbae Kim
Professor of Mechanical Engineering
Thesis Supervisor

Signature redacted

Accepted by: _____
Rohit Karnik
Professor of Mechanical Engineering
Undergraduate Officer

Mechanical Design of a Jumping and Self-Balancing Monopedal Robot

by

Evan Brown

Submitted to the Department of Mechanical Engineering
On May 22, 2018 in Partial Fulfillment of the
Requirements for the Degree of

Bachelor of Science in Mechanical Engineering

ABSTRACT

This project involved the design and fabrication of a self-balancing monopedal robot which is intended to be used as a platform for physically validating simulated risk network based control analysis. A precomputed risk network allows a robot to evaluate the risk that an action will lead to an imminent fall or lead to a state from which the robot will eventually fall after several jumps.[1] The physical implementation of the simulated robot will allow the theoretical boundaries of safety to be validated. If validated, risk matrix analysis will allow a system to be modeled such that the controller can modify control inputs which would lead falls. The results of physical testing will be used to refine the simulated model.

The robot was designed to be as simple as possible while still being capable of operating in three dimensions to study hybrid dynamics and underactuated locomotion. A mechanism with a direct kinematic relation to the output along with a static contact area was designed to allow the ground force profiles to be accurately controlled. In order to utilize the risk network, the force applied by the foot as well as the robot's take-off angle and rate of angular rotation at take-off are key parameters which must be measured and controlled. The robot was be optimized to precisely control these parameters rather than to achieve the longest or highest jump possible as is the objective of other studies.

Thesis Supervisor: Sangbae Kim
Title: Professor of Mechanical Engineering

[1] Wang, Albert, and Sangbae Kim. "Practical Network Based Approach for Computing Safety in Dynamic Systems." MIT, 2018.

Acknowledgements

I would like to thank Professor Sangbae Kim and Albert Wang for their input and advice throughout the course of this project. Albert Wang wrote the jumping simulation code, helped in part selection, and with the implementation of the electronics and control system. This project could not have been successful without his efforts. I would like to thank Prof. Sangbae Kim for the use of his lab space, tools, and materials. I would also like to thank the MIT Pappalardo Lab and their generous staff for the use of lab space, tools, and equipment.

Table of Contents

List of Figures

List of Tables

1. Introduction

1.1 Background

This project entailed the design and fabrication of a self-balancing monopedal robot which will be used to physically validate the results of a simulated risk network based control analysis. A precomputed risk network allows a robot to evaluate the risk that an action will lead to an imminent fall or will lead to a state from which the robot will eventually fall after several jumps.[2] The physical implementation the simulated robot will allow the theoretical boundaries of safety to be validated. If validated, risk matrix analysis will allow a system to be modeled such that controller or user inputs which would lead to instability can be identified. The results of physical testing will be used to refine the simulated model.

A literature review was conducted to evaluate existing jumping robotic platforms. In order to execute complex maneuvers, some robots are designed with multiple degrees of freedom.[3,4] Multiple degrees of freedom significantly complicate the control problem and will likely result in higher weight due to the larger number of actuators, thus limiting overall robot performance. In order to mimic the simulated robot most closely, a robot with a single degree of freedom jumping motion will be designed. Other existing devices which utilize a single degree of freedom leg mechanism are primarily designed for jumping in one direction.[5] Some mechanisms such as a scissor lift have one degree of freedom but still have high complexity. Although this mechanism is capable of creating linear motion, it has a large number of moving

---

[2] Wang, Albert, and Sangbae Kim. "Practical Network Based Approach for Computing Safety in Dynamic Systems." MIT, 2018.
[3] Arikawa, Keisuke, and Tsutomu Mita. "Design of Multi-DOF Jumping Robot." IEEE Conference Publication, Wiley-IEEE Press, May 2002, ieeexplore.ieee.org/document/1014358/.
[4] Ho, Thanhtam, and Sangyoon Lee. "Design of an SMA-Actuated Jumping Robot." IEEE Xplore, IEEE, 19 July 2010, ieeexplore.ieee.org/document/5513129/.
[5] Zuo, Guoyu, et al. "BJR: A Bipedal Jumping Robot Using Double-Acting Pneumatic Cylinders and Torsion Springs." IEEE Xplore, Wiley-IEEE Press, Aug. 2010, ieeexplore.ieee.org/document/5985845/.

parts and joints that complicate the design and create more points where energy will be lost to friction.[6] Robots which rely on linkages that provide a direct kinematic link between actuation and end effector motion are seen to be the most effective and applicable to this project. A variety of styles of linkages are used to generate a jumping motion.[7,8,9] The family of mechanisms used in these robots is seen in many animals such as frogs, grasshoppers, and kangaroos which are known for their jumping capabilities.[10] The feet of these animals tend to remain in contact with the ground for long periods of time so that a large amount of energy can be released such that a high takeoff velocity is achieved. The successful jumping robots in these studies mimic this behavior. In some of these mechanisms the contact point is relatively large and moves during the course of the leg motion. A moving contact area makes the force applied by the foot more challenging to control and is also not as easily generalized for use in multiple dimensions as some other mechanisms. This limitation is clearly seen in one of the studies where a robot which uses this style of mechanism is capable of generating a jumping motion "upwards" and "forwards".[11] Although capable of achieving a jump of many times its own height, this robot is not capable of jumping "backwards" let alone out of plane. In addition, this robot is not capable of controlling its orientation while airborne or capable of landing repeatedly such that multiple jumps may be executed in series. These shortcoming will be addressed by the design of the robot

---

[6] Zheng, Yili, et al. "Mechanical Design and Dynamics Analysis on a Jumping Robot." *Advanced Materials Research*, Trans Tech Publications, 27 Feb. 2012, www.scientific.net/AMR.476-478.1112.

[7] Li, Fei, et al. "Jumping like an Insect: Design and Dynamic Optimization of a Jumping Mini Robot Based on Bio-Mimetic Inspiration." Science Direct, Elsevier, 30 Jan. 2012, www.sciencedirect.com/science/article/abs/pii/S0957415812000025.

[8] Zhang, Jun, et al. "A Bio-Inspired Jumping Robot: Modeling, Simulation, Design, and Experimental Results." *Science Direct*, Elsevier, 12 Oct. 2013, www.sciencedirect.com/science/article/pii/S0957415813001645.

[9] Bosworth, Will, et al. "The MIT Super Mini Cheetah: A Small, Low-Cost Quadrupedal Robot for Dynamic Locomotion." IEEE Xplore, Wiley-IEEE Press, 2012, ieeexplore.ieee.org/abstract/document/7443018/.

[10] Li, Fei, et al. "Jumping like an Insect: Design and Dynamic Optimization of a Jumping Mini Robot Based on Bio-Mimetic Inspiration."

[11] Zhang, Jun, et al. "A Bio-Inspired Jumping Robot: Modeling, Simulation, Design, and Experimental Results."

for this project; however, the underlying design principles seen in these robots will be used to influence mechanism selection and the overall design of the robot.

A mechanism with a direct kinematic relation to the output along with a static contact area is preferable because it allows the force profile to be more accurately determined. In order to utilize the risk network the force applied by the foot as well as the robot's take-off angle and rate of angular rotation at take-off are key parameters which must be measured and controlled. The robot will be optimized to precisely control these parameters while still achieving a sufficient jump height to study interesting behaviors rather than to achieve the longest or highest jump possible as is the objective of other studies cited above.

The robot will be designed to interface with a testing rig that will allow data on the position and orientation of the robot to be collected as accurately as possible without relying solely on accelerometers and other onboard sensors that may tend to drift over time or be susceptible to noise. This rig will also ensure that testing is as safe and repeatable as possible. Testing using the robot developed in this project will initially be focused on simulated two dimensional cases which prove the viability of the risk network analysis. The results obtained in two dimensions can be readily generalized to three dimensions if the initial results are validated. Assuming initial efforts in two dimensions are successful, this robot will be applied to the three dimensional case. By making the design as generalized as possible, the robot may also be useful in future research into other relevant problems having to do with single legged jumping robots which were outside of the scope of this specific project. Design and construction of the testing rig as well as implementation of the full control system of this project proved to be outside of the scope of what was achievable during the semester over which this project was undertaken and will remain as areas of future work.

1.2 Motivation

The results of this project will be used by Albert Wang to physically validate the results of risk network control analysis. Once fabricated, the physical parameters of the robot will be fed into the simulation and then the results will be compared to observed behavior. This testing and comparison to simulated results is outside of the scope of this project. The objective of this project is to create a robust robot which can be completed and refined for use in future stages of the project as a part of the PhD thesis of Albert Wang.

1.3 Project Planning

Before beginning the design of this project a work breakdown structure was created to help identify key tasks. The work breakdown structure was made into a preliminary project Gantt chart. This chart was helpful for identifying availability as well as key milestones and deadlines. The initial Gantt chart created for this project is shown in Figure 1.

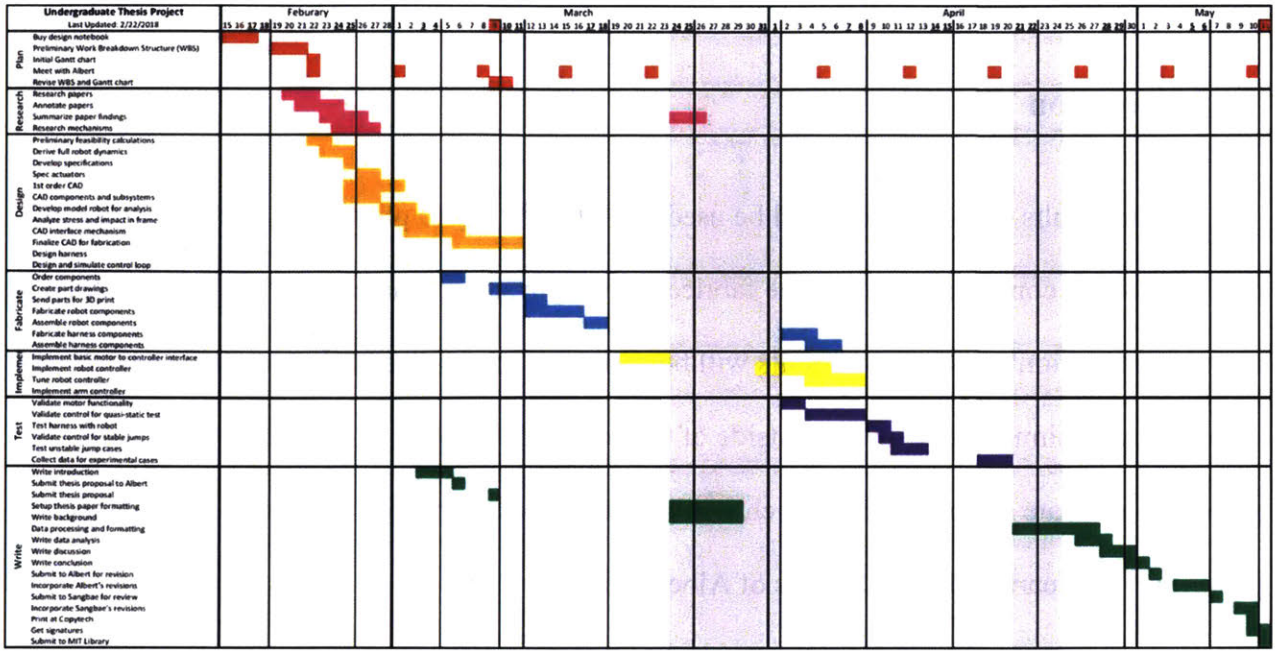

Figure 1: The initial Gantt chart developed from the work breakdown structure.

The initial Gantt chart was evaluated after completion of the project as a tool to analyze the project from a non-technical engineering management perspective.

2. Mechanical Design

After conducting research on current jumping robots and setting a tentative schedule for the project, the design phase of the project began. The design phase is where most of the work for this project occurred.

2.1 Specifications

For this project a set of specifications were developed to guide the design. Since the objective of this study is to develop a platform which will be able to act as a physical implementation of risk network analysis, robustness and controllability will be prioritized above

maximizing jump height. By keeping the design simple, the behavior can be fully understood and modeled in simulation.

In order to achieve acceptable jumping performance a specification was set that the robot must be able to jump twice the height of its body. Robots seen in review of the literature were seen to jump many times their own body height, so achieving this level of performance seemed reasonable despite sacrifices made in jump performance in order to achieve enhanced control. In order to test extreme "risky" behaviors the robot needs to be able to recover from a tilt angle of at least 45 degrees.

In order to implement the robot featured in the simulations, the design must have some kind of leg which moves linearly to apply force to the ground.

Since the robot is designed to do be used with a harness which is for safety as well as to aid in data collection, the robot does not need to be a self-contained platform. This will allow me to fully maximize the capabilities of the robot.

2.2 Mechanism Selection

For the mechanism that is designed for the foot, force must be controlled. The robot will control the force profile of the foot during contact with the ground. Data on the force that the foot applies will be used in future work as a comparison to the analytical model and simulation. Before designing specific mechanisms, many mechanisms and actuators were considered for generating linear motion. Mechanisms or actuators that were considered include voice coils, rack and pinions, multiple styles of cams, the pantograph linkage, delta robot configuration, scissor lifts, and lead screws.

Given the insight provided by the literature review and considering robustness and ease of fabrication as primary design considerations the pantograph design was selected. The pantograph mechanism allows the foot to stay in contact with the ground for long periods of time with a fixed point of contact while also having a direct kinematic relationship between input and output motion. In order to generate linear motion with this mechanism the upper leg segments must rotate in a coordinated manner such that the angle bisector between the legs remains vertical for all leg rotation angles. Although independent motors with feedback could be used to achieve this result, a physical connection and transmission system controlled by a single motor was selected. This greatly simplifies the controller needed to operate the robot by linking leg motion directly to the rotation of a single motor in a one to one mapping.

2.3 Kinematics

In order to understand the pantograph mechanism, the kinematics of the mechanism were derived. By making this analysis general, the key parameters such as the length of the linkages were able to be modified and optimized during the design process.

The hip joint is defined to rotate in a 180 degree arc which results in the legs moving between parallel and anti-parallel configurations. The angle between the vertical and the legs is shown for both the parallel and anti-parallel configurations and defined as the angles φ_1 and φ_2 as shown in Figure 2 in addition to a trapezoid which represents the body of the robot. In Figure 2 the shading of the joints are shown in the key of Figure 2. Leg extension is defined as the variable L is the vertical distance between the axis of the hip joints and the foot joint. The leg is shown at minimum extension L_{min} in the anti-parallel configuration and at maximal extension L_{max} in the parallel configuration in Figure 2.

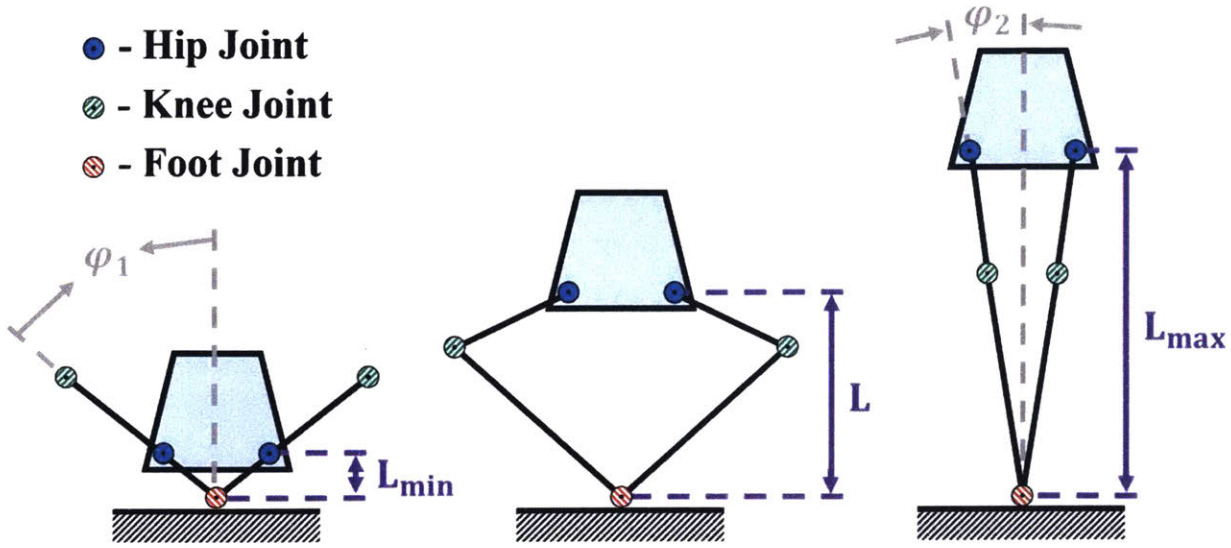

Figure 2: The definition of the angle phi offset from vertical which is used in later derivations. The anti-parallel configuration is shown at left with the parallel configuration at right. The trapezoid represents the "body" of the robot.

The values for each of the variables defined in Figure 2 were calculated as a function of the chosen system design variables which were the length of the upper leg segment L_1, length of the lower leg segment L_2, and the distance from the hip joint to the mechanism's axis of symmetry L_3 as shown in Figure 3. This mechanism has one degree of freedom. The variable θ, defined as the amount of clockwise rotation from the line defined a φ_1 in Figure 2, is the state variable which was chosen to determine the configuration of the leg. This was a logical selection as the position and torque of the mechanism are controlled by a motor which is linked to rotation at the hip joint. The leg extension L is defined as a function of θ and of geometric parameters as shown in Figure 3.

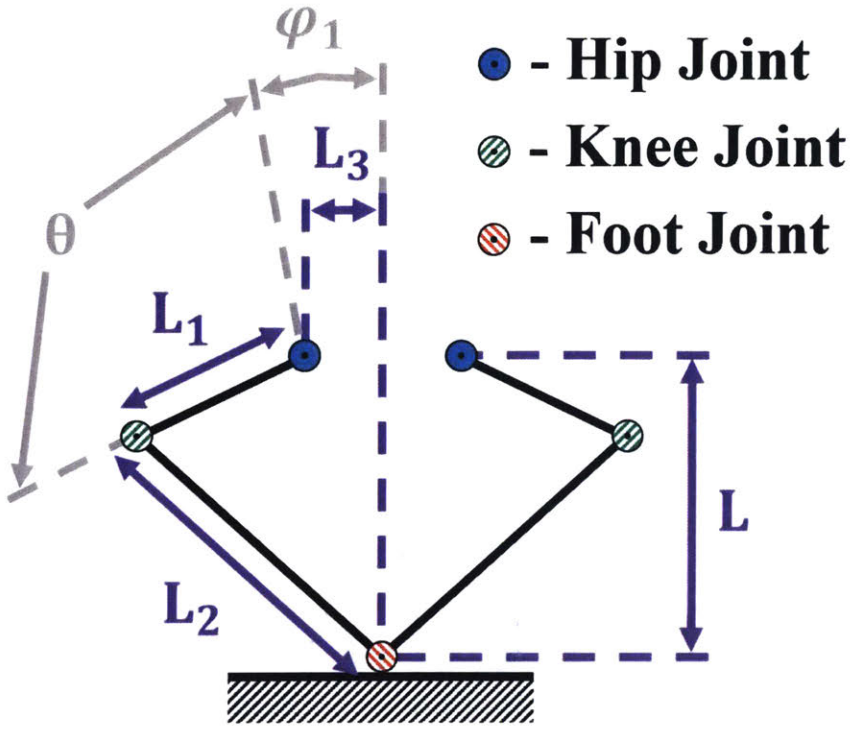

Figure 3: The linkages of the leg mechanism are positioned in an arbitrary configuration defined by the state variable θ. The value of the leg extension L is taken as a variable dependent on the shown geometric parameters and θ.

The derivation of the angles φ_1 and φ_2 as defined in Figure 2 are shown in Equation (1) and Equation (2) respectively.

$$\varphi_1 = \sin^{-1}\left(\frac{L_3}{L_2 - L_1}\right) \tag{1}$$

$$\varphi_2 = \sin^{-1}\left(\frac{L_3}{L_2 + L_1}\right) \tag{2}$$

The minimum and maximum leg extensions are also functions only of geometric parameters. The derivation of these values is shown in Equations (3) and (4).

$$L_{min} = \sqrt{(L_2 - L_1)^2 - (L_3)^2} \tag{3}$$

$$L_{max} = \sqrt{(L_2 + L_1)^2 - (L_3)^2} \tag{4}$$

As discussed during the selection of this mechanism, the upper legs will be linked by a transmission which ensures that the foot remains constrained to a linear path. In this transmission, gearing will be applied to optimize motor performance. This gearing effects the relationship between the angle of the motor and leg extension. The gear ratio between the motor and the transmission will be defined as G. The gear ratio and the geometric parameters will be used later when selecting a drive motor and as key driving variables that determine the design of the system. The rotation angle at the hip joint θ is linear related to the angle of rotation at the motor θ_m as shown in Equation (5).

$$\theta = \frac{\theta_m}{G} \tag{5}$$

To preserve generality while assessing available motors and components a general equation was derived which relates motor rotation angle θ_m to leg extension L as a function of general parameters discussed above as shown in Equation (6). Leg extension is defined to be equal to L_{min} when θ is equal to zero which places the legs in the anti-parallel configuration. When the legs are at max extension (parallel configuration) then $\theta = \pi - \varphi_1 + \varphi_2$ which can be derived from geometry and is consistent with Equation (6).

$$L = \sqrt{{L_2}^2 - \left(L_3 + L_1 \sin\left(\frac{\theta_m}{G} + \varphi_1\right)\right)^2} - L_1 \cos\left(\frac{\theta_m}{G} + \varphi_1\right) \tag{6}$$

The leg extension curve described by Equation (6) is shown in Figure 4 with sample geometric parameters. In Figure 4 $L_1 = 1$, $L_2 = 2$, $L_3 = 0.5$, and $G = 2$. Figure 4 shows leg extension as a function of the angle of the drive motor. The point of minimum extension is marked with a green star and the point of maximum extension is marked with a red square.

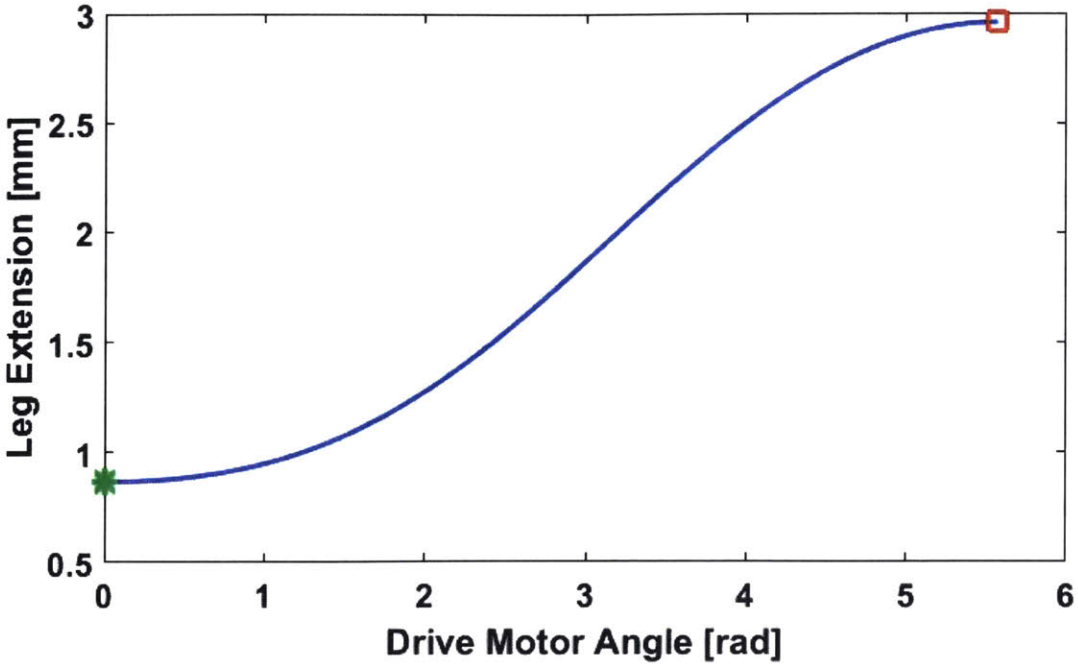

Figure 4: Leg extension plotted as a function of the angle of the drive motor. The points of minimum and maximum extension are marked with a green star and red square respectively.

Note that the relationship between motor angle and leg extension is non-linear. The slope of the curve in Figure 4 represents the effective gear ratio between the motor and the leg extension. Near minimum and maximum leg extension the slope is close to zero. This means that a change in motor angle has little effect on the motion of the leg. In the middle, the slope is large. This means that small changes in motor angle cause a large amount of leg extension.

This general shape is advantageous for use in a jumping because it has a variable gear ratio through the motion of the mechanism. When landing from a jump a large amount of force is required to slow and reverse the momentum of the robot from the previous jump. Assuming the robots lands with the leg at low extension the very flat slope of this curve means that the output force of the motor is magnified, thus decreasing the amount of torque the motor must be capable of providing in order to achieve high force output. The steeper slope of the curve around its

center allows for high speed output. This means that the motor speed can be slow such that the output torque of the motor is high. The relative high velocity of the output means that the robot can achieve a high enough velocity to achieve takeoff.

2.4 System Dynamics

Since the robot is capable of jumping, there is no single dynamics equation which governs its behavior. The robot may be in contact with the ground or may be airborne. When designing this system it was most important to consider the dynamics which relate to the jumping motion while the robot was in contact with the ground. Key assumptions are shown in the list below and then discussed and justified in greater detail below.

- Static center of mass independent of leg position
- Negligible leg motor angular momentum
- Reaction wheels spin at low speeds
- Dynamics for different tilt directions are decoupled

By making an assumption that the mass of the legs would be small as compared to the mass of the body of the robot, the position of the center of mass will change relatively little as a function of leg extension while airborne. Additionally, the assumption was made that the angular momentum caused by the drive motor spinning to move the legs while airborne would be small. Because the motor has to traverse a relatively small range of angular motion it will not be spinning at high speeds. Additionally, since the motor will both accelerating and the decelerating once it repositions, these effects should cancel on short time scales. In addition, a properly designed control loop for the reaction wheels will reject any slight angular disturbance caused by the drive motor. Since the leg motion is linear, the speed and torque of the reaction wheels have no effect on the leg extension.

Although there are interdependencies between the leg motion and the reaction wheels, the dynamics can be largely decoupled. When in contact with the ground, the length of the leg extension influences the reaction wheel dynamics because the robot pivots about the point where the robot's foot contacts the ground. Variable leg length means that the distance from the point of contact of the foot with the ground to the center of mass of the robot will change.

While in the air, dynamics are simpler as the robot rotates about its center of mass which is assumed to be stationary due to the low mass of the legs and the lack of external forces acting on the robot. Although physical constants such as the moment of inertia may be different between the θ and φ tilt directions, the underlying dynamics for the two reaction wheels is identical, so a derivation of the dynamics for only the θ direction will be conducted. It will be assumed that the dynamics and control of the θ and φ tilt angles are decoupled. This decoupling assumption is valid because the reaction wheels rely on reaction torques to create system stability rather than gyroscopic effects. DC motors are capable of producing the most torque at low velocities, so the control loop will be designed with the reaction wheels operating around angular speed. Because the speed of the reaction wheels will be low, any gyroscopic effects which would cause the dynamics of the tilt angle to be coupled will be neglected.

In this section the coordinate system for the robot will be defined, then the dynamics equations which govern its motion for the leg while in contact and the reaction wheels both when in contact with the ground and while airborne will be derived. After the dynamics have been derived the initial specifications will be applied to select motors and transmission components.

2.4.1 Coordinate System

In order to allow the robot's behavior to be as generalized as possible, the location and orientation of the robot will be defined in three dimensional space. The position of the foot of the

robot is defined using the coordinates x,y, and z. The coordinate z is defined to be zero when the robot's foot is in contact with the ground. This location is taken as the origin for a spherical coordinate system where R represents the distance from the origin of the coordinates to the center of mass of the robot. Positive rotation about the x axis as defined by the right hand rule is defined to be positive θ. Similarly, positive rotation about the y axis is defined to be positive φ. Figure 5 shows the robot in an airborne configuration with coordinates defined as discussed above.

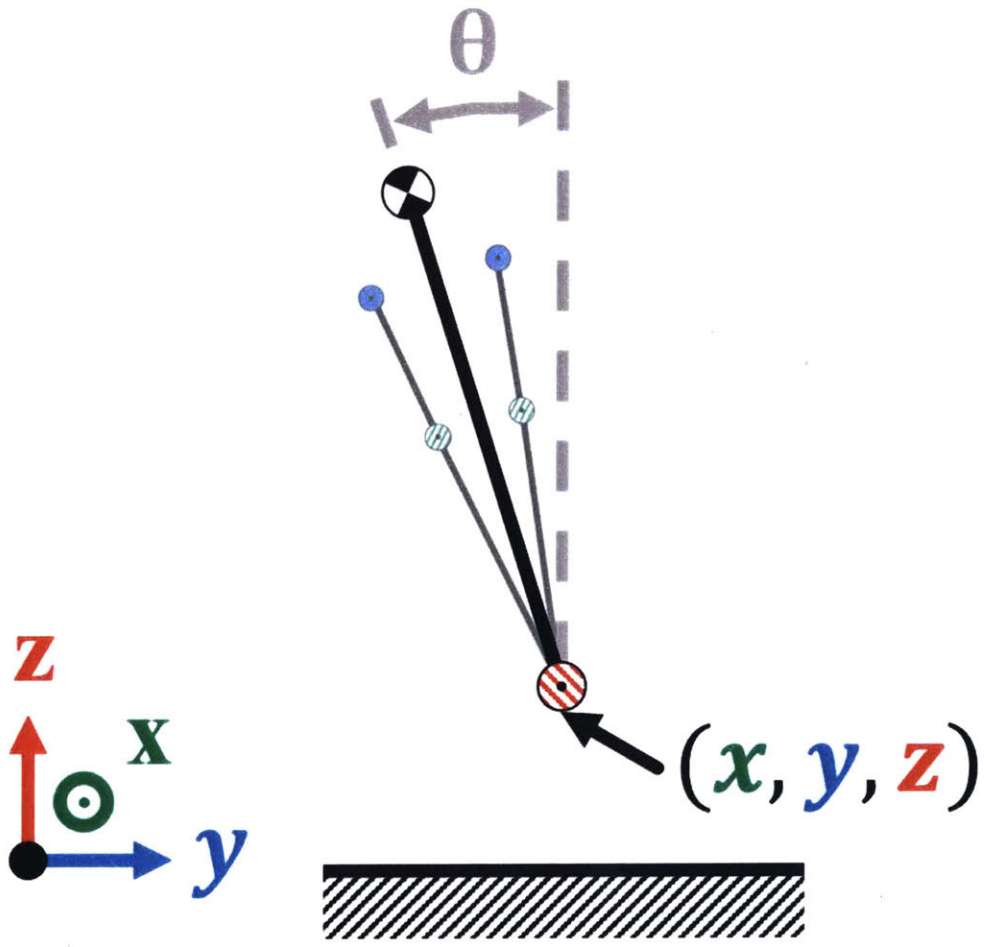

Figure 5: The coordinates system axis are defined at such that the origin is in the plane of the ground. The coordinates x,y, and z define the position of the bottom of the foot of the robot. Positive θ is shown as the positive rotation about the x axis.

Figure 6 shows a view rotated 90 degrees about the z axis from Figure 5 where the remaining coordinates are defined. The shadow of the robot mechanisms are shown in both figures for context. Note that rotation about the z axis is not defined. This degree of freedom cannot be controlled by the robot and should be negligible as no significant torques act along this axis.

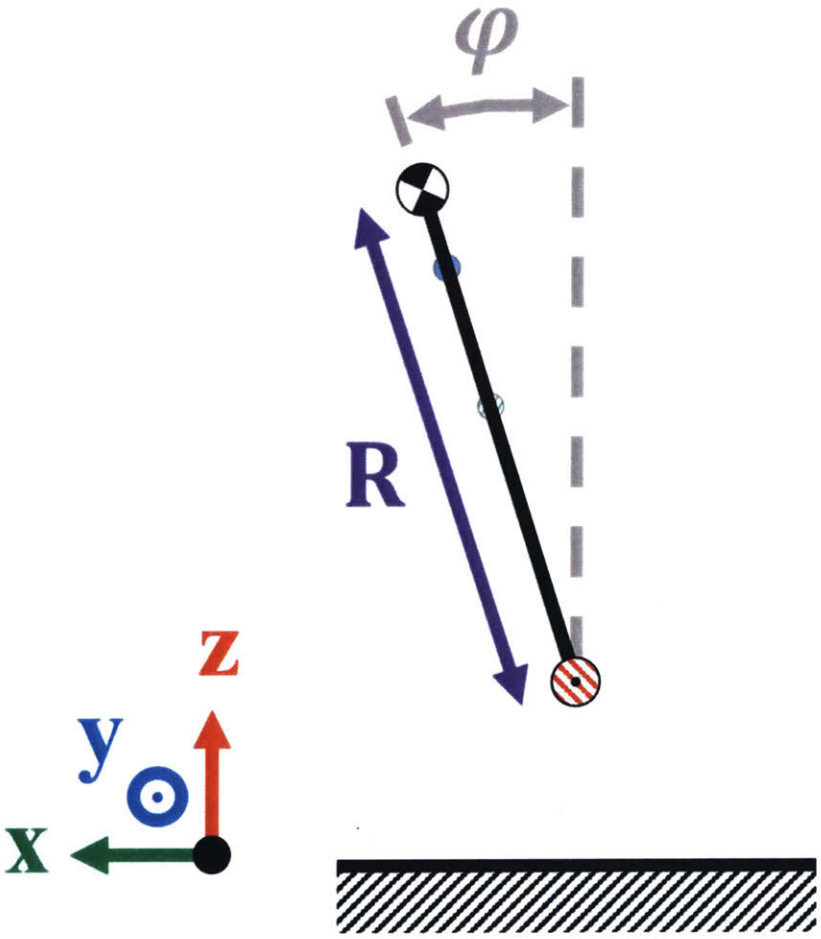

Figure 6: The remaining coordinates used to define the robot's orientation are shown. R represents the difference between the bottom of the foot and the center of mass. The angle φ is positive rotation about the y axis.

The location of the hip joints will be fixed relative to the center of mass, thus R can be defined as the sum of the leg extension L plus the parameter L_b which represents the in-plane distance between the center of mass and the line which intersects both hip joints as shown in Figure 7.

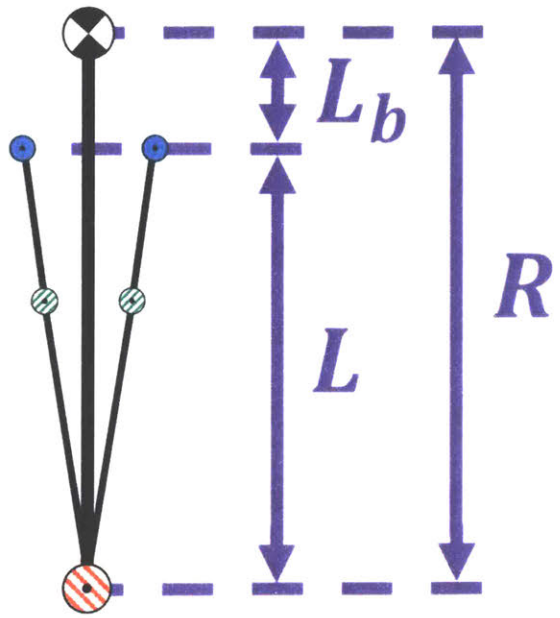

Figure 7: The coordinate R is the sum of the fixed geometric parameter L_b which relates the position of the center of mass to the hip joints and the length of leg extension L.

The relation in Figure 7 is shown in Equation (7).

$$R = L_b + L \tag{7}$$

2.4.2 State Variables

The robot is designed to have three motors which means that its state can be defined by three variables and their derivatives. The chosen state variables are the angle of the drive motor θ_m, the angle of the reaction wheel with its spin axis parallel to the x axis $\theta_{f\theta}$, and the angle of the reaction wheel with its axis of rotation parallel to the y axis $\theta_{f\varphi}$. These three states can be

used to control R, θ, and φ directly, while the variables x,y, and z are controlled by changing these states in a coordinated manner as this is an under-actuated system.

2.4.3 Leg Dynamics While Airborne

As detailed above, it will be assumed that the dynamics of the leg are governed only by the inertia of the system motor and the legs. The inertia of the motor (I_m), the inertia of the system (I_s), and the friction losses in the transmission (b) which provide damping will be considered. The governing dynamics equation is shown in Equation (8) with the state variable of drive motor angle (θ_m) with the motor torque (τ_m) as the input.

$$(I_m + I_s)\ddot{\theta}_m = \tau_m - b\dot{\theta}_m \tag{8}$$

The legs will be designed to be as lightweight as possible while also keeping the as much mass concentrated close to the point of rotation as possible. Thus it is likely that the inertia of the motor will be much greater than the inertia of the rest of the system. There will also be loses in the transmission due to friction which will add damping to the system; however, this should also be small. The total inertia of the system and the damping imposed by friction will be challenging to estimate analytically. These parameters would be best determined once the robot is constructed using a technique such as dynamic signal analysis to characterize these parameters. The transfer function between motor angle and motor torque is shown in Equation (9).

$$\frac{\theta_m}{\tau_m} = \frac{1}{s\big((I_m + I_s)s + b\big)} \tag{9}$$

Since no external forces act on the leg while the robot is airborne, the assumption that repositioning is nearly instantaneous is reasonably accurate for most operating regimes.

2.4.2 Leg Dynamics While Contacting Ground

When in contact with the ground the robot experiences reaction forces applied to the foot. Force parallel to the direction of motion of the leg will be considered while shear forces which are absorbed by the leg structure or used to maintain the no-slip constraint between the foot and the ground. The torque that the reaction force creates is dependent on the parameter θ_m due to the variable gear ratio of the mechanism as shown in Equation (10).

$$(I_m + I_s)\ddot{\theta}_m = \tau_m - b\dot{\theta}_m - \frac{dL}{d\theta_m}F_{contact} \tag{10}$$

Contact force is the parameter which is most relevant to measure and control for this robot. The force is directly related to the state of the robot and the input motor torque as designed.

2.4.5 Reaction Wheel Dynamics While Contacting Ground

While in contact with the ground the robot rotates about the contact point. It will be assumed that the contact point is stationary. Although the foot on which the robot stands will have some radius, this dimension will be minimized such that any motion caused by the foot rolling without slipping while in contact with the ground is minimal.

A simplified model of a variable length bar pinned at one end (the ground) with a mass at the other end will be used in this analysis. The bar length represents the distance from the pivot point to the center of mass of the system (R). This simplifies the model of the robot to a standard inverted pendulum as shown in Figure 8. The forces which act on the system are gravity (g) and the torque provided by the motor driving the reaction wheel (τ_r).

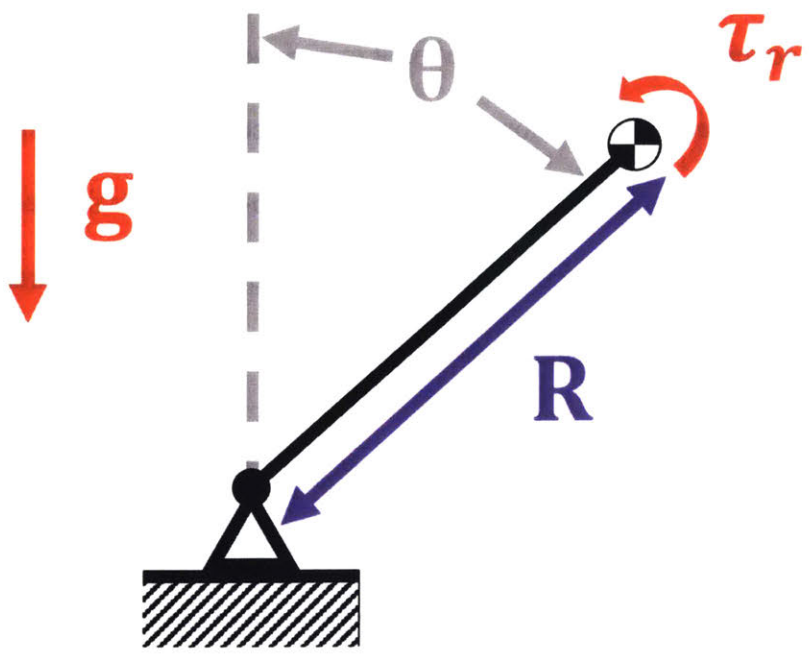

Figure 8: The planar inverted pendulum model is used as the model for robot dynamics while the robot is in contact with the ground.

The moment of inertia of the system is dependent on the length of the bar (R) and the moment of inertia of the body about the center of mass (I_b). The moment of inertia of the system about the pin joint is calculated using the parallel axis theorem as shown in Equation (11).

$$I = I_b + mR^2 \tag{11}$$

The dynamics equations using the moment of inertia calculated in Equation (11) are shown in Equation (12).

$$I\ddot{\theta} = gR\sin(\theta) + \tau_r \tag{12}$$

Since the robot must be capable of jumping at extreme angles, the small angle approximation that is valid up to about 15 degrees of tilt is not valid. Thus the full non-linear dynamics of the system must be considered.

2.4.6 Reaction Wheel Dynamics While Airborne

While airborne, the robot rotates about its center of mass. Gravity acts at the center of mass and thus generates no external torque. The rotational speeds of the robot are small, so the effect of air resistance will be neglected. The dynamics equation is simple as the reaction wheel motor creates a reaction torque on the body while no other torques act on the system. The dynamics equation for the robot's body is shown in Equation (13).

$$I_b\ddot{\theta} = \tau_r \tag{13}$$

2.5 Motor Specification

When working to select motors for the robot, the dynamics equations above in addition to additional equations below were used to predict the torque requirements of each of the motors. The two most important specifications set for the system concern jumping height and the angle from which the robot can correct itself back to an upright position.

2.5.1 Leg Motor Specification

The specification on jumping is that the robot must be capable of jumping twice the height of its body. In order to simplify the estimations for the purpose of selecting a motor it was assumed that the force from the foot is constant. Choosing the motor based on the minimum torque means that the output force will actually be much higher when the leg is near minimum or

maximum extension. It will be assumed that this force acts over the distance from minimum to maximum leg extension.

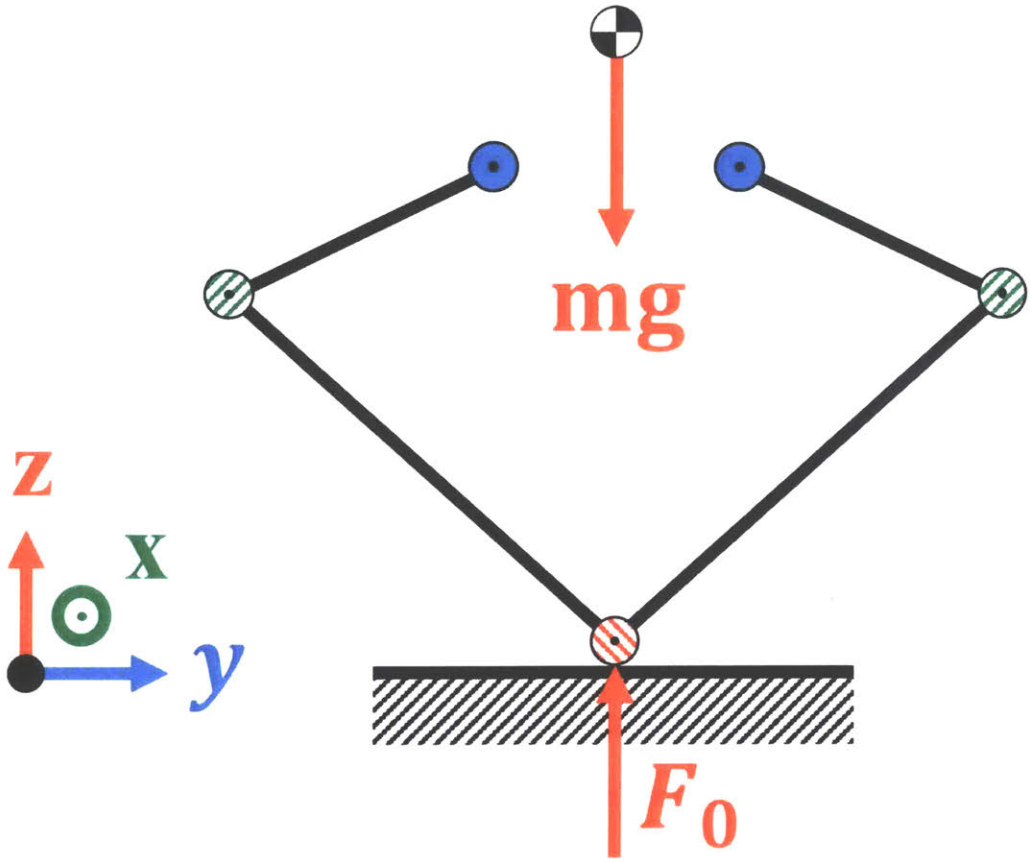

Figure 9: The robot shown in a jumping configuration with the force provided by the leg and gravity shown.

The jump height which results will be analyzed from an energy perspective. The work input to the system is provided as torque from the drive motor that is translated into linear motion of the foot via the pantograph leg mechanism. When built, the motion of the leg may be slightly less than this theoretical displacement; however, this will likely be small and will still allow a motor with appropriate parameters to be selected. When designing the leg mechanism, considerations will be made which allow for as large a range of motion as possible such that

neglecting this difference is appropriate. The work input to the system will be equated to the potential energy of the system at its maximum jump height as shown in Equation (14).

$$F_0(L_{max} - L_{min}) = mgz_{max} \tag{14}$$

Solving for z_{max} as in Equation (15) provides a more useful specification which more directly involves parameters such as force and geometric parameters of the robot.

$$z_{max} = \frac{F_0(L_{max} - L_{min})}{mg} \tag{15}$$

Since this specification is relative to the height of the robot, making the mechanisms as compact as possible as to minimize the height of the robot's body will be important.

In order to select a motor, the parameter F_0 must be written as a function of geometric and motor parameters. In order to calculate the output force of the mechanism as a function of input torque the principle of virtual work will be applied as shown in Equation (16).

$$\tau_m * \delta\theta_m = F_0 * \delta L \tag{16}$$

Solving for F_0 yields the result in a relation involving the slope of the kinematics equation ($\frac{dL}{d\theta_m}$) which relates leg extension to motor angle for the leg mechanism in section 2.3 Kinematics and the motor torque as seen in Equation (17).

$$F_0 = \frac{\tau_m}{\frac{\delta L}{\delta\theta_m}} \tag{17}$$

In order to be conservative with the estimation, the slope will be taken at the midpoint of the curve where the slope is maximized, thus minimizing F_0. The drive motor will operate at relatively low speeds meaning that the torque output will be roughly equivalent to the stall torque. A motor with roughly twice the calculated stall torque τ_{ms} will be selected in combination with geometric and transmission parameters to provide a sufficient factor of safety

to account for friction and a smaller range of motion for the leg. The motor specification are solved for in terms of system parameters in Equation (18).

$$\tau_{ms} = \frac{mgz_{max}}{L_{max} - L_{min}} * \left(\frac{\delta L}{\delta \theta_m}\right)_{max} \tag{18}$$

Due to the complexity of the kinematic relation, the slope will be calculated using a numerical approximation of the slope around the drive motor angle in Equation (19).

$$\overline{\theta_m} = \frac{G}{2}(\pi - \varphi_1 + \varphi_2) \tag{19}$$

The approximation of the slope will be taken numerically using a value for Δ which is several orders of magnitude less than the value of $\overline{\theta_m}$ as in Equation (20).

$$\left(\frac{\delta L}{\delta \theta_m}\right)_{max} = \frac{L(\overline{\theta_m} + \Delta) - L(\overline{\theta_m} - \Delta)}{2\Delta} \tag{20}$$

The motor selected was the Maxon EC 60 flat motor model 411678. This motor has a stall torque of 4.18 N*m.

2.5.2 Reaction Wheel Motor Specification

In order to test the threshold of "risky" behaviors, the robot must be capable of recovering from at least a 45 degree angle of tilt. In order to maintain reasonable response it will be assumed that the reaction wheel motor operates at half of its no-load speed or less to maintain the potential of creating high reaction torques. This will also result in a low angular velocity for the reaction wheels thus avoiding significant gyroscopic effects as was assumed earlier. The motor speed is dependent on the size of the reaction wheel; however, by ensuring the reaction wheel has a large enough moment of inertia later in the design process a motor can be selected

now based on torque alone. At 45 degrees of tilt, it will be assumed that the reaction wheel motor operates at half of its stall torque as shown in Figure 10.

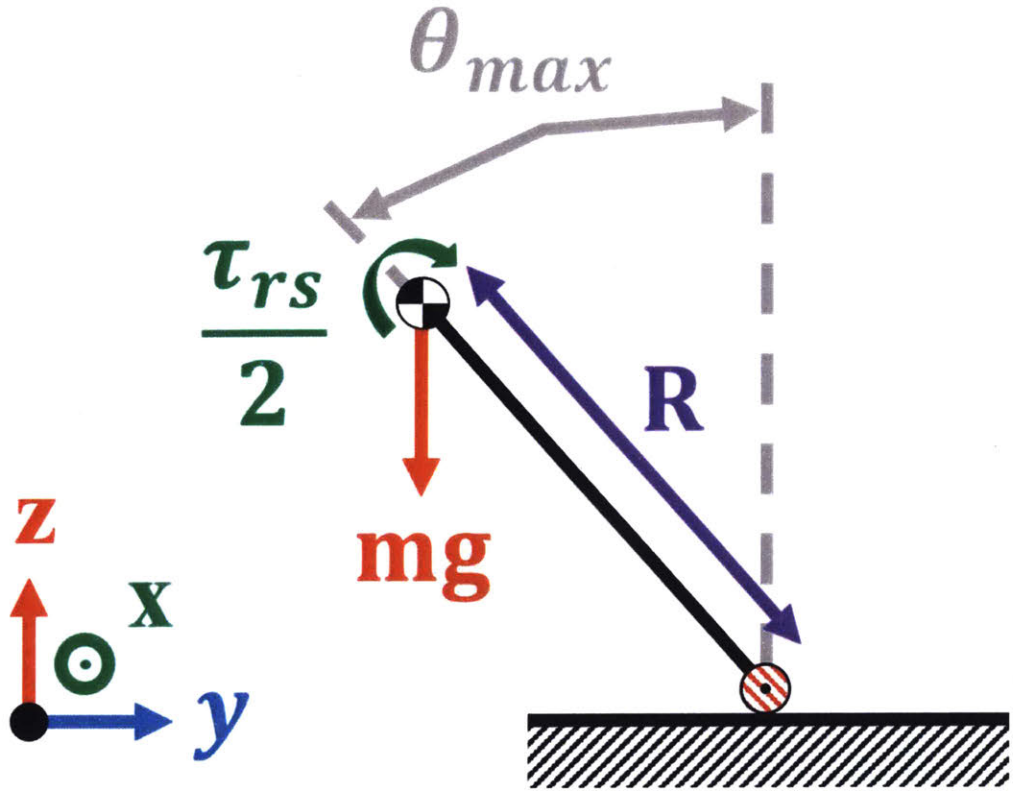

Figure 10: The inverted pendulum model shown at the maximum recoverable angle with the reaction wheel motor providing a reaction torque of half of the stall torque. It will be assumed that the leg is at half of its maximum extension.

In order to provide a reaction torque which causes negative angular acceleration the condition in Equation (21) must be met.

$$mgR\sin(\theta) < \frac{\tau_{fs}}{2} \tag{21}$$

The value of θ will be taken to be θ_{max} at 45 degrees. The leg will be assumed to be at half of its max extension. When in a static balancing situation, the robot would tend to keep its leg retracted as to be prepared for a jump and to minimized its moment of inertia about the contact point with the ground. Thus the only case where the robot needs to balance with an

extended leg is during the course of the jumping motion. Due to the changing gear ratio of the leg mechanism, the robot will takeoff around the midpoint of leg extension. Since the robot will have its leg extended to half of full extension or less during the majority of its operation, this condition is a conservative assumption. The condition for motor stall torque is given in Equation (22).

$$\tau_{fs} > \sqrt{2} m g R_{L=L_{max}/2} \tag{22}$$

The motors that were chosen were the Maxon EC 45 flat motor model 339285 with a stall torque of 1.1 N*m and a no load speed of 660 rad/s.

2.6 Detail Design

As an overall strategy, equations were used extensively in the development of the CAD model of the robot. One advantage of using equations is that they allow repeated dimensions to be updated simultaneously across the entire assembly. Additionally, key parameters such as those used in the specifications formulas as well as the dimensions of off the shelf components are used to drive the dimensions of the assembly.

In order to make static stability using the reaction wheels possible, the center of mass must be kept as close directly above the contact point as possible. This constraint meant that components with large mass such as the motors and reaction wheels were placed as close to the center line as possible or were placed so as to balance each other.

The distance between axles was determined using the gear pitch diameter and belt length as driving parameters. The distance between axles was determined as a function of the diameters

of the two pulleys to which it was connected and the overall belt length. These key quantities are shown in Figure 11.

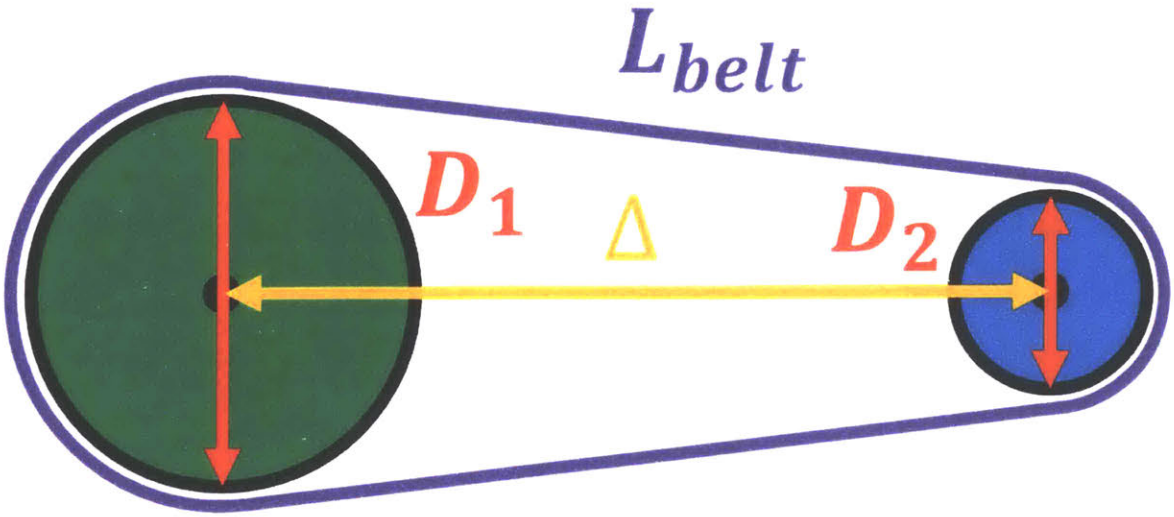

Figure 11: The diagram used to calculate the axle separation between a set of pulleys of different diameters with a fixed belt length.

Although any three of the parameters shown in Figure 11 determine the fourth, the axle separation was chosen as the driven parameter because it could be easily modified whereas the other three parameters were dependent on the parts that could be sourced. Additionally it would be simple to modify the axle separation on future iterations to adjust belt tensioning. Equation (23) shows the relation used in the CAD model to approximate axle separation.

$$\Delta = \frac{1}{2}\left(L_{belt} - \frac{\pi}{2}(D_1 + D_2)\right) \tag{23}$$

By applying these formulas, maximizing compactness, and maintaining symmetry of components such as the drive motor the configuration shown in Figure 12 was developed. This design uses three belts and a set of gears to keep the drive motor on the center line while achieving the coordinated opposing rotational motion at the hip joints required by the pantograph mechanism. Additionally, the motor was positioned as low as possible to keep the center of mass

of the robot as low as possible. Note that the objects depicted in Figure 12 are not located in the same plane. The rough outline of the drive motor is shown in the center in transparent red. The belt which connects the motor to the transmission is shown in red. This belt is a 6 mm wide 2.03 mm (MXL) pitch belt with 54 teeth. The set of gears which create the opposing motion of the two sides of the leg are shown in transparent green with a black outline. The belts that connect to the hip joints are shown in purple are 6mm wide 3 mm (HTD) pitch belts with 73 teeth. The ratio between the transmission and the hip joint is 36 to 14.

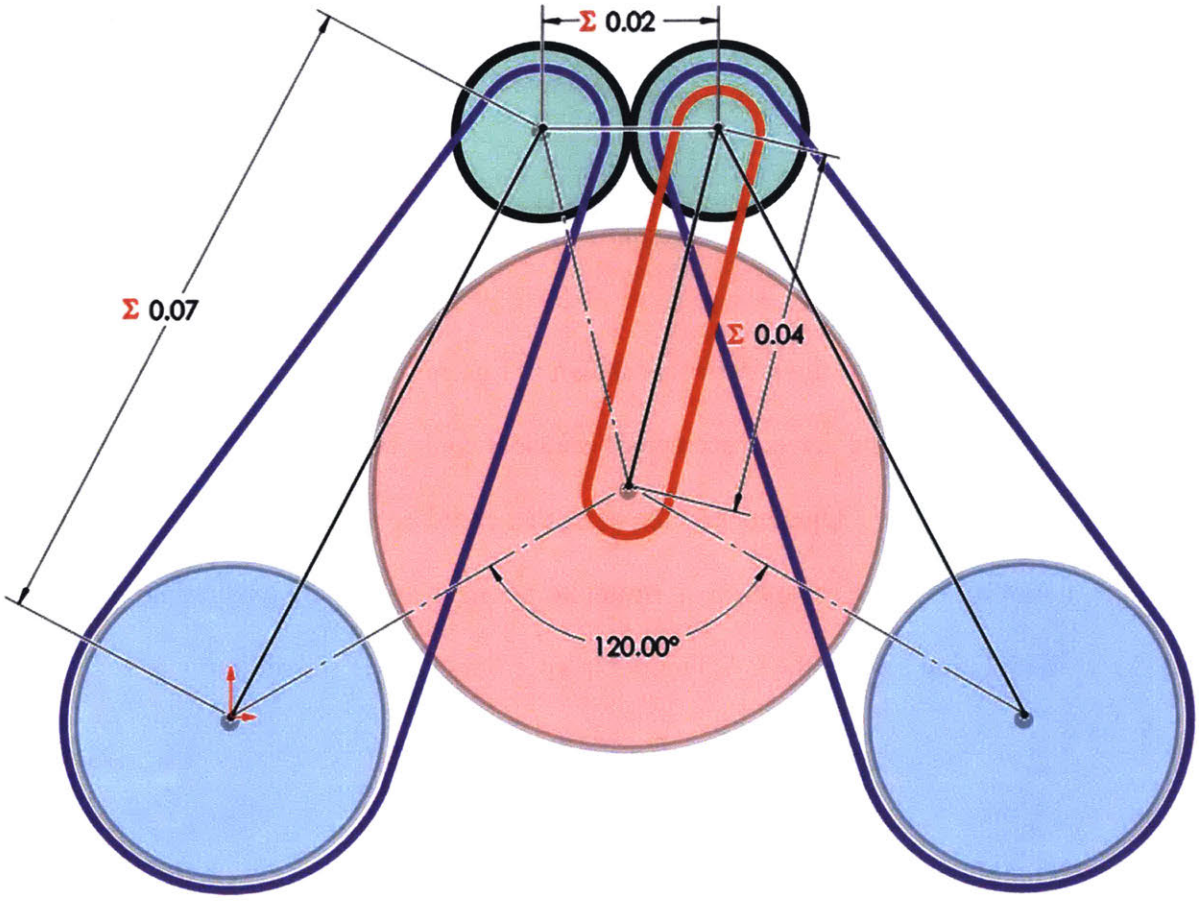

Figure 12: The transmission system of the robot is driven by equations and symmetry. The driving dimensions are shown on the figure. The outlines of key transmission components including the drive motor (transparent red), drive belt (red), gears (transparent green with black outline), hip belts (purple), and hip pulleys (transparent blue) are shown. The design was optimized to make the configuration compact.

In order to simplify fabrication and make the robot easy to disassemble and service pulleys and gears with locking hubs were selected. Some design tradeoffs were made to accommodate the components which were available. The completed CAD model of the transmission system is shown in Figure 13. Components with the same coloration are mechanically connected via gears or belts.

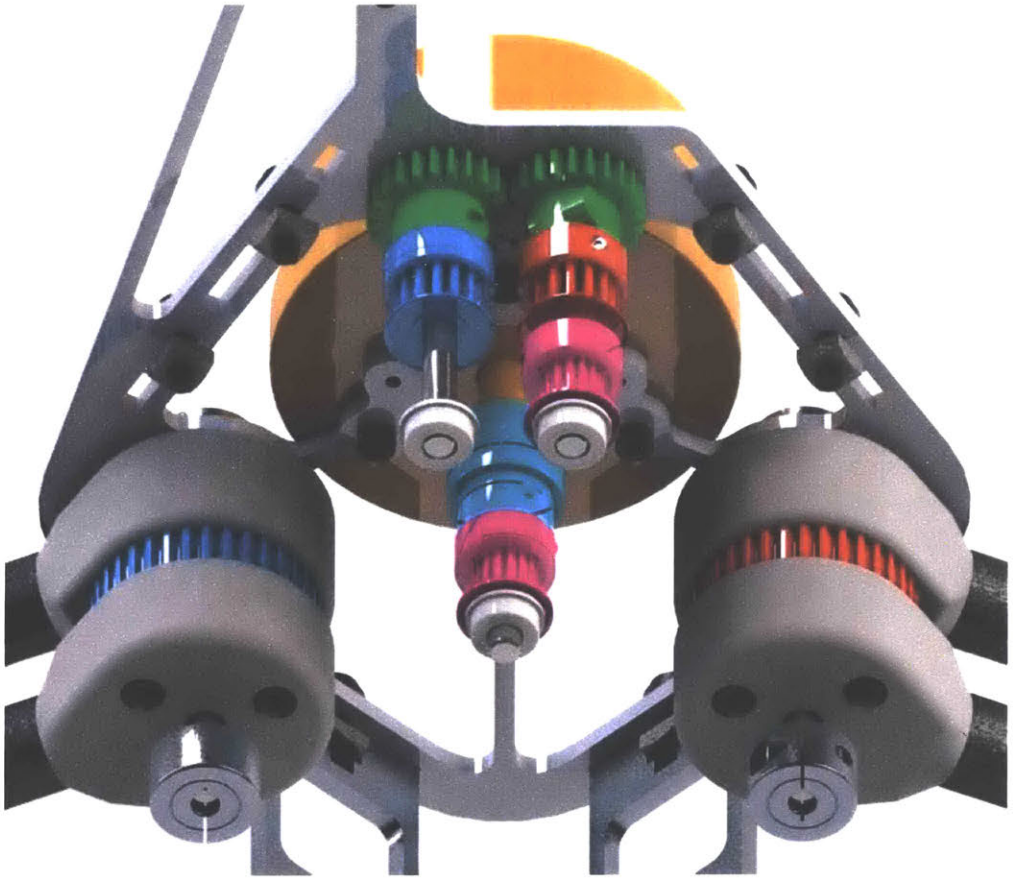

Figure 13: The transmission system of the robot. The drive motor (orange) shaft is stepped down to a smaller shaft size by a coupler (cyan) to accommodate the drive pulley pair (purple). The gears (green) create the opposed motion of the legs to create linear motion at the foot. The geared shafts are connected to the hip joints by the pulley pairs (blue and red).

To support the shafts in the transmission from both sides a parallel plate design was chosen. Bearings press fit into the parallel plates to reduce friction on the shafts as shown on the ends of the shafts in Figure 13. In order to minimize weight, Aluminum was selected as the

material for the frame. To create a frame with high rigidity, a mortise and tenon style was used to connect perpendicular plates.[12] Tenons on cross pieces were designed to fit into corresponding mortise slots on the two main panels. Clearance holes on the main panels allow for screws to thread into square nuts held in "t" shaped cutouts on the cross pieces. These screws clamp cross pieces firmly to the main panels taking normal loads. Shear loading is transferred to the mortise and tenon portion of the cross pieces. By locating cross pieces roughly perpendicular to each other, both directions of planar shear can be handled by the frame. By transferring forces to the frame, the transmission and attached reaction wheels are not loaded by the high impact loads experienced during the jumping process. The mortise and tenon style of construction is shown in Figure 14.

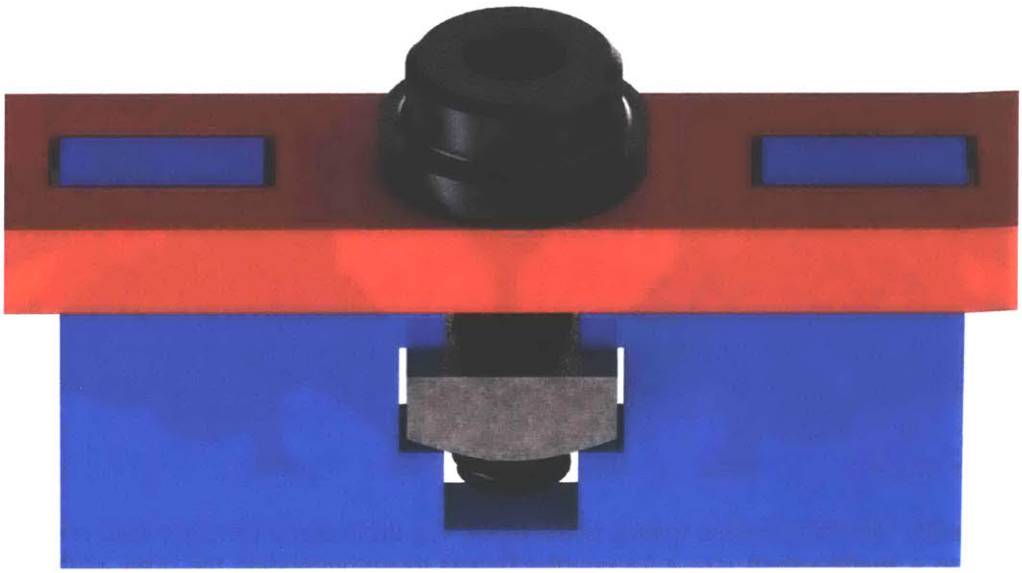

Figure 14: The mortise and tenon style construction used to join perpendicular components cut on the water jet. The cross piece is shown in blue while the main plate is shown in red. The screw and square nut are in tension while the tenons (blue) fit into mortise slots in the main plate (red) take shear loads.

[12] Design inspired by past work in the MIT Biomimetics Robotics Lab

In order to minimize the mass of the robot the reaction wheel motors spin with the reaction wheel, contributing to the reaction wheel moment of inertia. A custom locking hub was designed to mount the reaction wheel rings to the outer diameter of the motor casing such that the rings of the reaction wheel are concentric with the motor. Because the hub is adjustable it can be moved laterally on the motor's outer diameter within a small range as an adjustable mass to fine tune the balance of the robot once assembled. The reaction wheel rings were made from stainless steel which has a much higher density than aluminum and thus provides a higher moment of inertia for the reaction wheels. The reaction wheel assembly is shown in Figure 15.

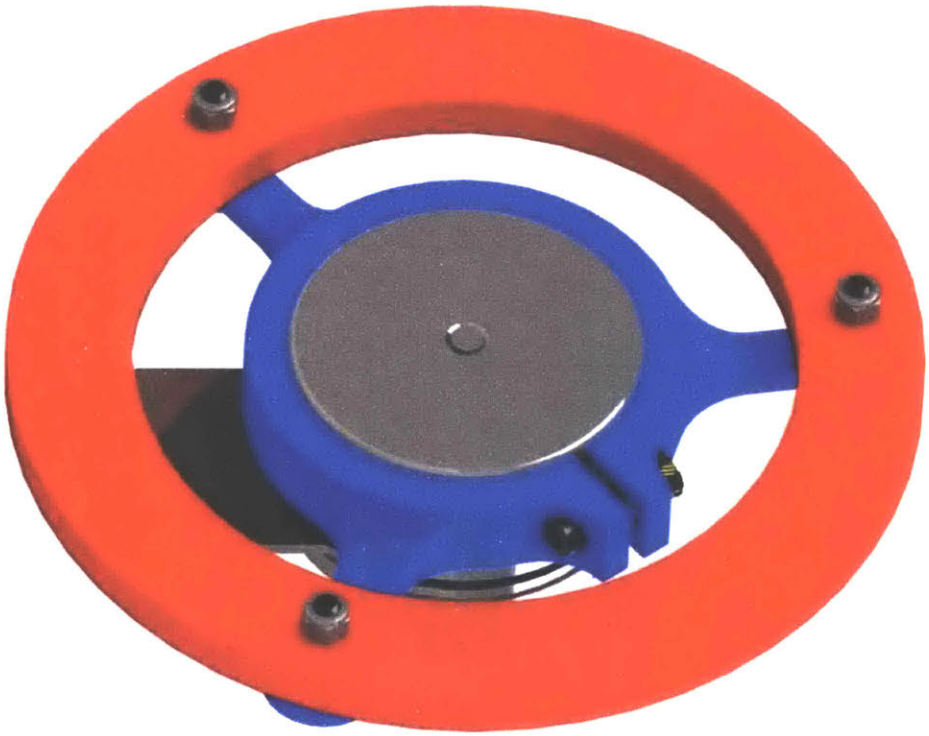

Figure 15: The reaction wheel is composed of two rings (red) which are made of stainless steel that bolt to the custom locking hub (blue) which clamps to the outer diameter of the reaction wheel motor.

The first reaction wheel is located parallel to the plate where the drive motor was positioned to counterbalance the weight of the drive motor. Due to the tight packing of the

transmission near the center of the robot, the second reaction wheel was positioned vertically above the transmission orthogonal to the first reaction wheel to keep it vertically above the center of mass. The reaction wheels are positioned orthogonally such that stability in the θ and φ tilt directions can be achieved. It was determined that placing the second reaction wheel on the centerline was more important than having a lower center of mass. The reaction wheels along with the center of mass location are shown in the Solidworks model in Figure 16. The light blue lines in the front view and side view extend vertically upwards from the contact point at the bottom of the foot. Note that the center off mass is well centered above the contact point. The distance from the estimated center of mass to the vertical line which intersects the contact point is 1.4 mm. Given that small changes are likely to occur during fabrication, and given that the minimum value of R is 130 mm this deviation is very small and will not have a significant impact on the performance of the system.

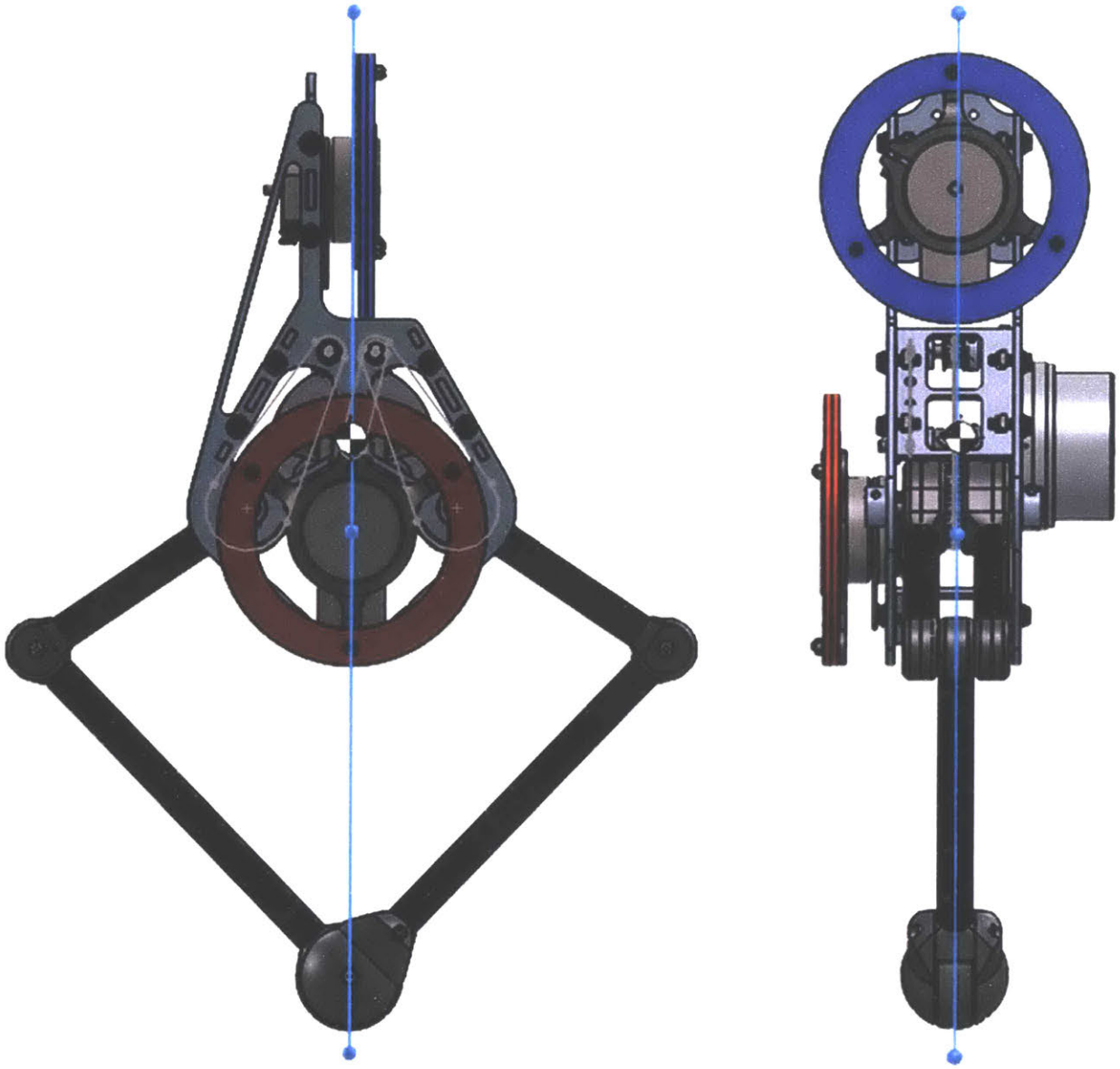

Figure 16: The reaction wheels are positioned orthogonally to provide stability in the θ and φ tilt directions. One reaction wheel (red) serves to counterbalance the drive motor while the second (blue) is positioned above the transmission system to keep the center of mass above the contact point. The vertical light blue line is vertically above the contact point and is located very close to the estimated position of the center of mass.

To save weight and maximize the performance of the robot, large cutouts were made on the main body plates as well as the side plates shown in Figure 17. Material along lines where force was transferred was preserved. Cutouts were conservative because a complete stress

analysis of the parts was not conducted. In future iterations a material cutout optimization software would be employed.

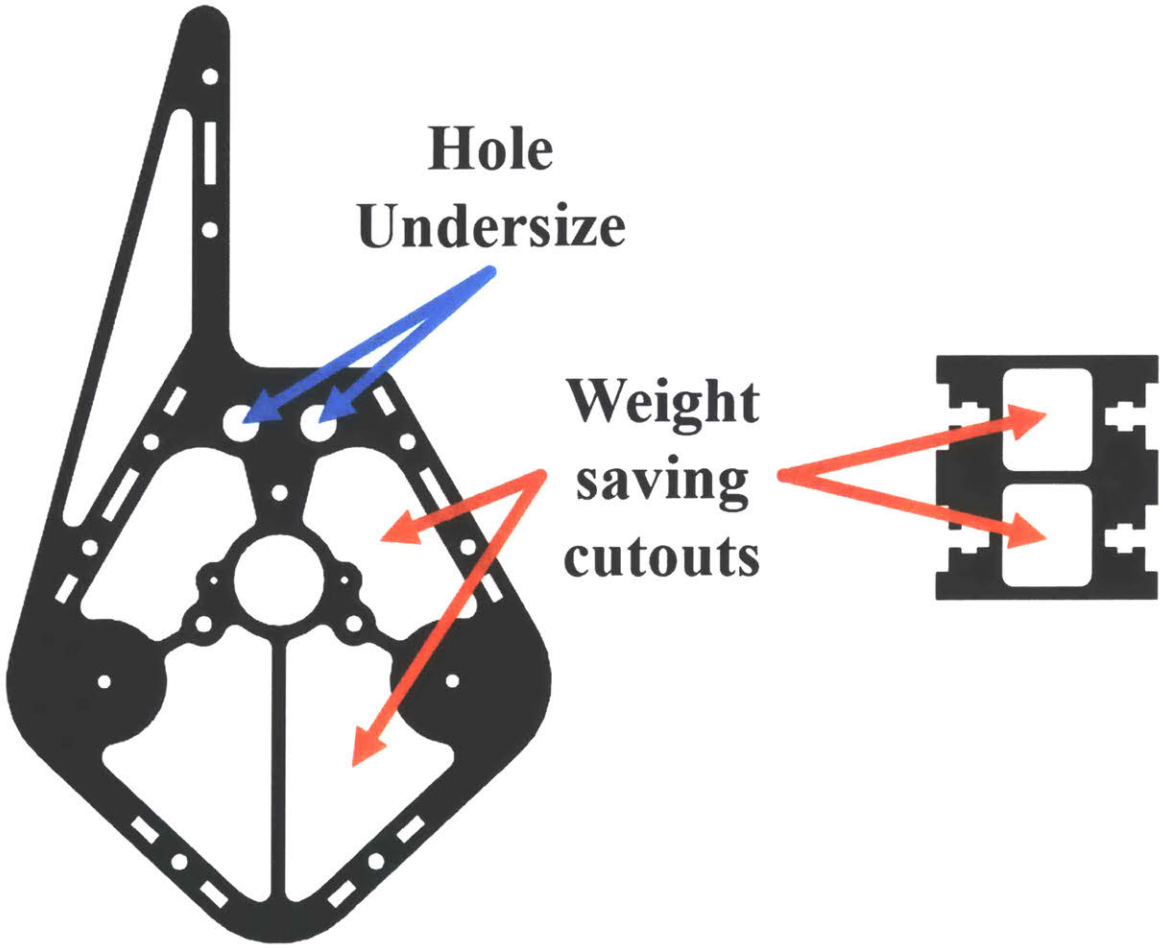

Figure 17: Cutouts were created to save weight. Material was preserved along lines where large amounts of force will be transferred such as around the perimeter of the frame. Some of the features were cut on the waterjet undersized and then post-processed to allow for press fits or for tapped holes.

In order to create the complex geometry of the body panels the waterjet was used. The waterjet tolerance is appropriate for creating clearance holes features such as the slots along the perimeter. Some of the holes in the waterjet components were designed as press fits or as tapped holes. Although a waterjet could meet the dimensions and tolerances needed it may have taken testing and iteration to refine these dimensions. Given the tight schedule of the project and since

this part will not be mass produced, the decision was made to undersize the holes when waterjetting and then post-process the part by drilling out these holes to the precise size needed. With this method the waterjet determines the position of the holes while post-processing determines the dimensions.

A similar strategy was employed for 3D printed parts where holes that required a press fit were undersized and then drilled out to the proper diameter. The reaction wheel hub and leg joints of the robot were 3D printed. This helped to keep these components lightweight and allow iteration on the design to occur rapidly. Leg joints were designed to fit inside of carbon fiber tubes which compose most of the leg's structure. 3D printed components were attached to the carbon fiber tubes using epoxy. Most leg joints contain roller bearings. Joints were printed in multiple parts such that the bearings could be press fit inside before assembly. Parts of the joint were then held together using an adhesive or via the use of bolts and heat set inserts. Bolts and heat set inserts have the advantage that the joint can be disassembled which is helpful during the prototyping phase; however, due to its lower weight, attaching joint parts using an adhesive would be preferred in a future design iteration. A cross section view of the hip joint in Figure 18 shows the 3D printed joint components in red and green and the center pulley in cyan. These components are held together with a pattern of bolts and heat set inserts, one of which is visible. The roller bearings are shown in blue and are designed to press fit in between the halves of the 3D printed components.

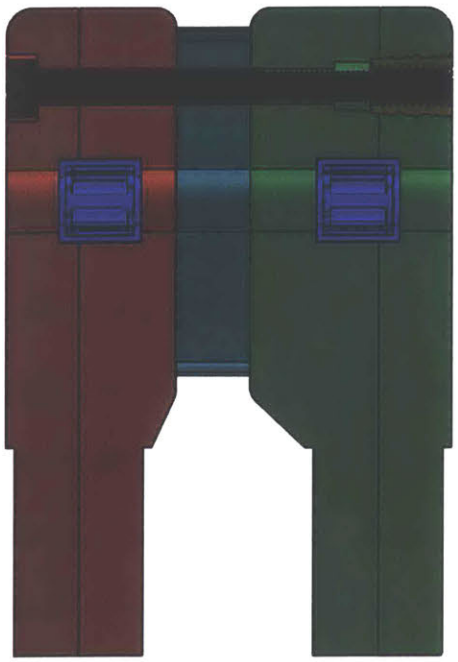

Figure 18: A cross section view of the hip joint. Note the roller bearings press fit in between halves of the 3D printed joint components shown in red and green. The assembly is held together by a pattern of bolts and heat set inserts.

An interface which will be used for attaching the testing rig was included in the design. This pattern of holes is located at the top of the robot such that the testing rig would not impact the operation of the robot. By providing a set attachment method an adapter could easily be created if an alternative mounting design proves advantageous. The test rig mounting holes are shown in red in Figure 19.

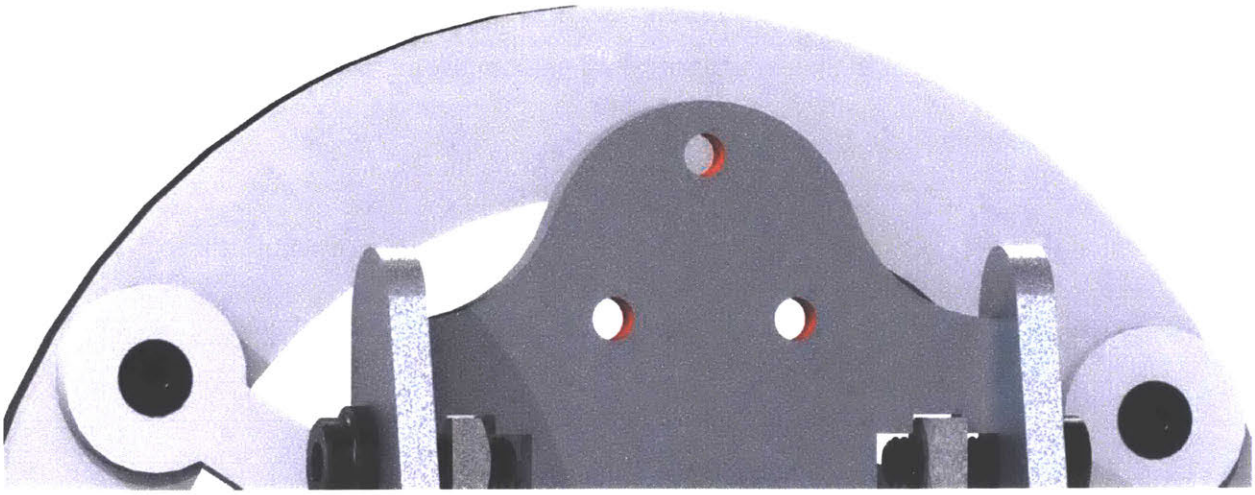

Figure 19: Mounting holes located near the top of the robot allow for attachment of a testing rig. The mounting holes are shown highlighted in red.

These features are designed to provide for future work on the project. In addition because this part is relatively small, a new part could be waterjet to fit in this location which had a different mounting configuration without having to change any of the other aspects of the design.

2.7 Simulated Behavior

As additional verification before fabrication, simulations were conducted to verify the performance of the robot using a version of the code which is used to conduct the risk network analysis.[13] In the Solidworks model a material was assigned to each part such that an accurate assessment of the mass of the robot could be made. Hand calculations were used to determine the reaction wheel moment of inertia given the density ρ, thickness t, reaction wheel motor inertia I_{rm}, inner and outer radii R_i and R_o as in Equation (24).

[13] Simulation code written by Albert Wang.

$$I_{reaction\ wheel} = I_{rm} + \pi\rho t\left(R_o{}^4 - R_i{}^4\right) \tag{24}$$

The parameters used in the simulation based on dimensions and measurements taken from Solidworks are in Table 1.

Table 1: Parameters used in simulation of the robot from the larger risk matrix analysis code.

Variable in Paper	Variable	Variable in Code	Value	Units
Robot mass	m	m_B	2	kg
Reaction wheel mass	m_f	m_f	0.368	kg
Robot moment of inertia	I_θ	I_B	0.01020538	$kg * m^2$
Reaction wheel moment of inertia	I_f	I_F	0.000705181	$kg * m^2$
Minimum leg extension	L_{min}	L_min	0.13	m
Maximum leg extension	L_{max}	L_max	0.335	m
Hip to COM distance	L_b	L-L_min	0.027	m
Reaction wheel motor torque	τ	tau	1.1	$N * m$
Leg extension force	F_0	FLeg	59.14	N

The resulting trajectory from the simulation is shown in Figure 20. Note that the center of mass achieves a height of 0.436 meters which is more than twice the initial height of the center of mass at 0.157 meters.

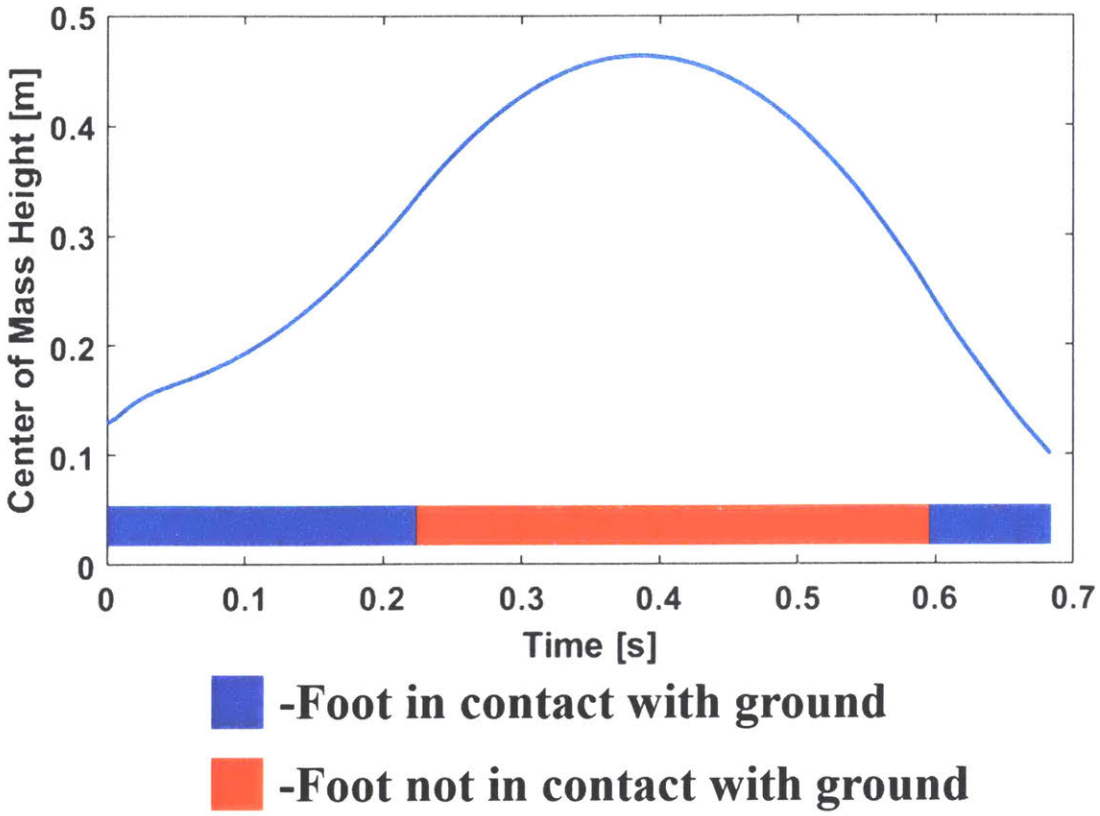

Figure 20: The resulting simulated jump profile using the parameters in Table 1. The maximum jump height is 0.463 meters.

When the leg is fully retracted the height of the robot is 0.288 meters tall. Assuming a vertical jump, the top of the robot (rather than the center of mass) reaches a height of 0.62 meters. This peak is more than twice the initial height of the robot thus satisfying the jump hieght specification.

The motion of the reaction wheel is also calculated by the simulation. In order be near the stall torque where the motor torque is greatest, the angular speed of the reaction wheel should be below 330 radians per second which is half of the no load speed of the reaction wheel motors. The speed of the motor is well below this value for the simulated jump.

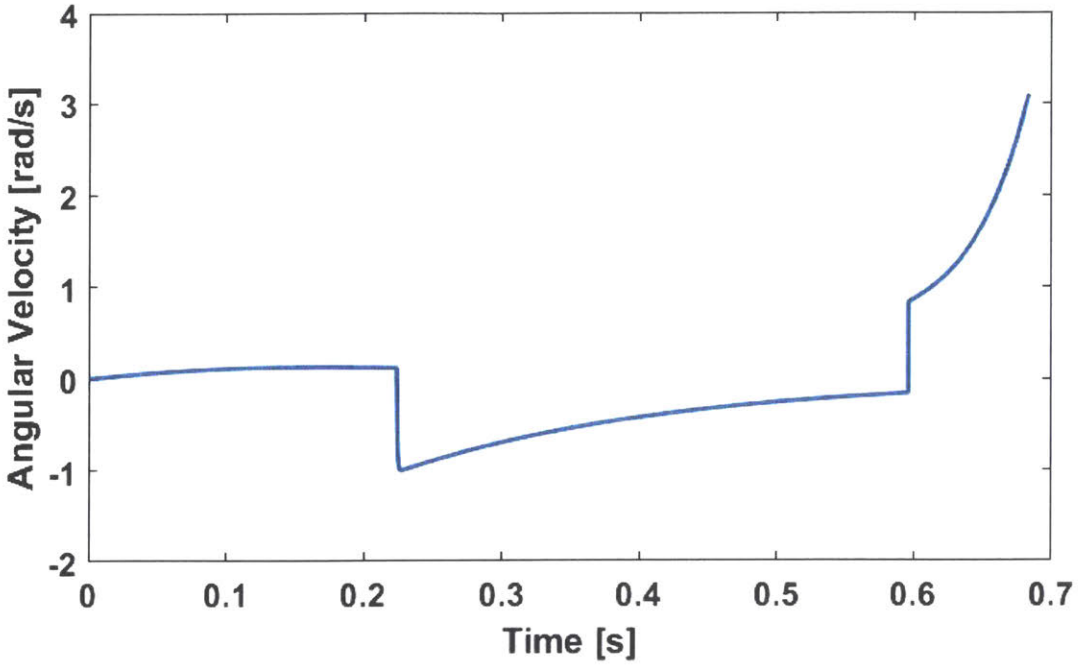

Figure 21: The reaction wheel angular velocity for the simulated jump. Since the simulated jump is near to vertical the angular speed is well below half of the reaction wheel motor's no load speed of roughly 330 rad/s.

2.8 Sensors

The motors selected for this design have some built in sensing capabilities. In addition to this sensing encoders were added to the shafts of each of the motors to provide more accurate measurements of motor position and velocity. In order to simplify the system the same encoders were chosen for each of the three instances in which encoders were used on the robot. Encoders with through holes were installed to maintain the compactness of the design. The encoder is shown installed on the upper reaction wheel in Figure 22.

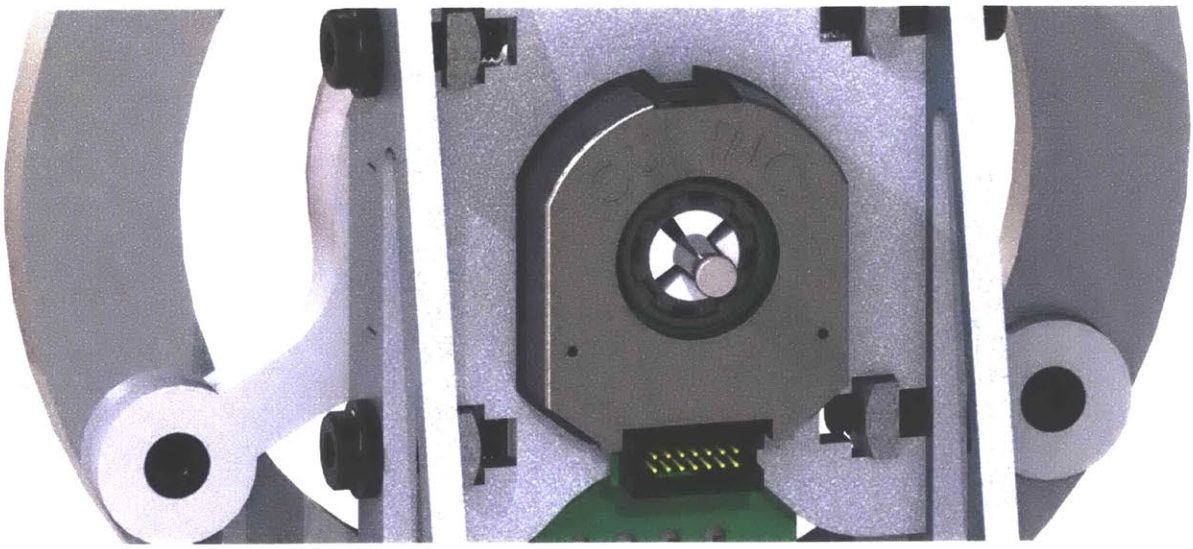

Figure 22: The encoder on the upper reaction wheel is shown located on the motor output shaft. The encoder attaches to the frame with a pair of bolts which attached to tapped holes in the cross support section of the frame. The other encoders are attached by a similar method.

In addition to the encoders that sense the motor positions, an on board accelerometer is used to measure the angles θ and φ of the robot.

2.9 Assembled Robot

The completed fabrication of the robot including several key components discussed above are shown in Figure 23 through Figure 28.

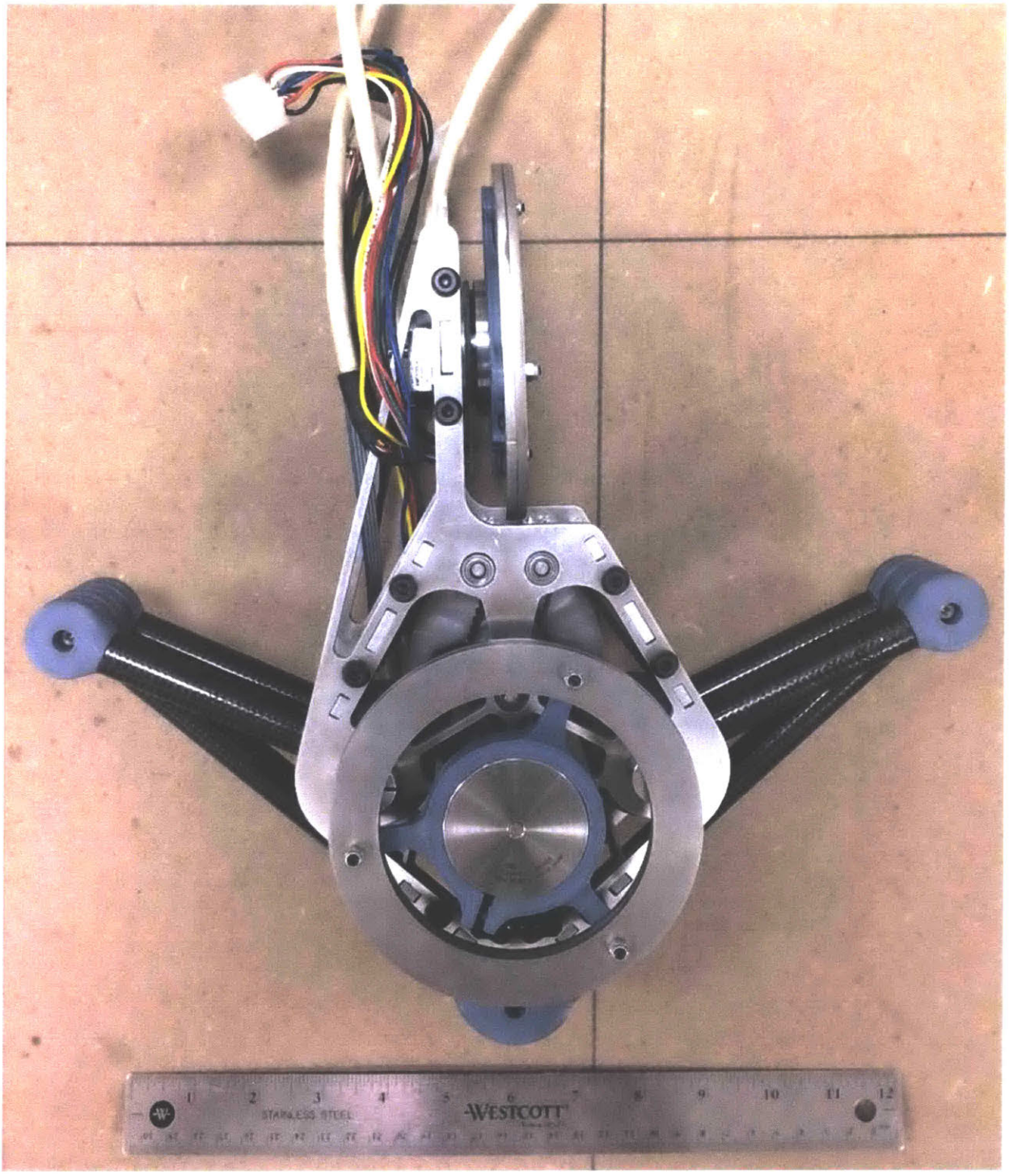

Figure 23: The completed robot shown with legs fully retracted. Note the position and orientation of the two large reaction wheels.

Figure 24: The completed robot shown from the side orientation.

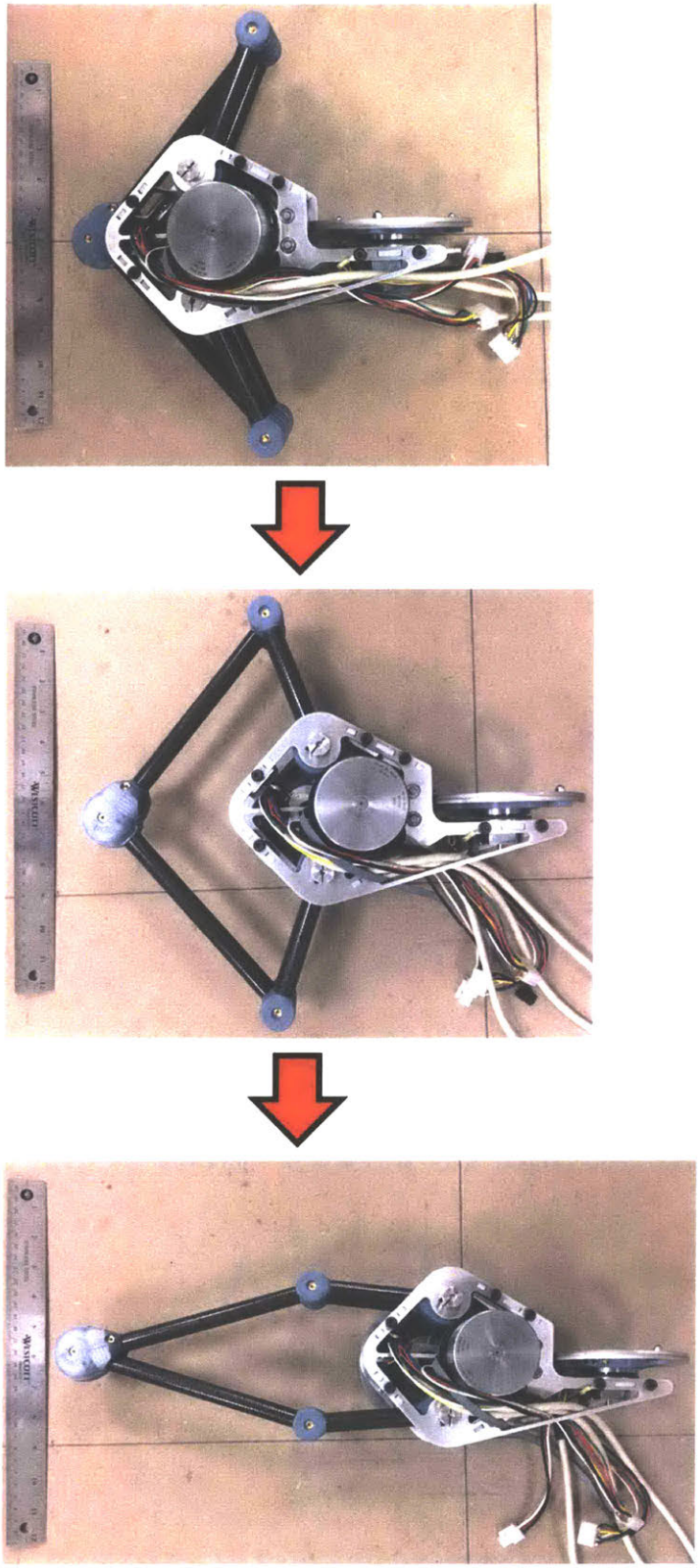

Figure 25: The completed robot shown with the leg positioned in poses which would be a part of the jump progression.

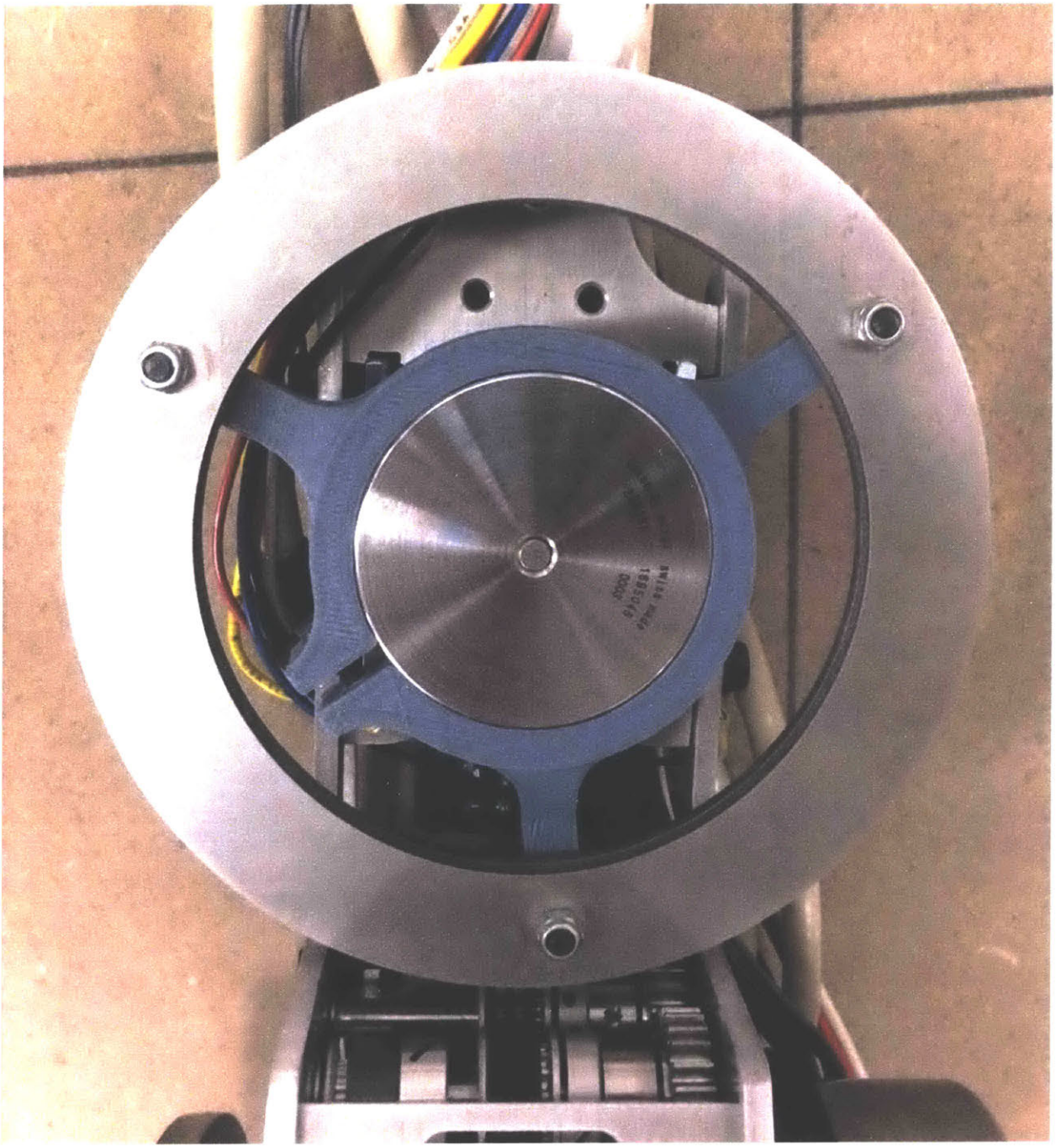

Figure 26: A close up view of one of the reaction wheels shown with the locking hub. The gears and some other belts and pulleys which make up the transmission can be seen near the bottom of the photo.

3. Controller Design

The two degree of freedom inverted pendulum is a standard controls problem. Under the assumption that gyroscopic effects are minimal, the problem can be decoupled into a control loop for rotation in the θ direction and rotation in the φ direction. The moment of inertia will be different around these two axis; however, the controller design will be very similar. In this section the control loop for rotation in the θ direction will be analyzed and then later applied to the φ direction. The control system design and implementation was not completed for this project.

The derivation of the equation of motion for the single degree of freedom inverted pendulum was shown in Equation (12). The non-linearity caused by the sine function makes analysis more challenging. Initially, the equation of motion will be linearized. This assumption will allow the robot to be controlled within 15 degrees of vertical before the linear approximation's accuracy declines. The linearized equation of motion is shown in Equation (25).

$$I\ddot{\theta} = gR\theta + \tau_f \tag{25}$$

Taking the Laplace transform allows the transfer function between θ and τ_f to be determined as shown in Equation (26).

$$\frac{\theta}{\tau_f} = \frac{1/I}{s^2 - gR/I} \tag{26}$$

This transfer function has a pole in the right half plane, indicating instability. The pole zero plot of the open loop transfer function is shown in Figure 27.

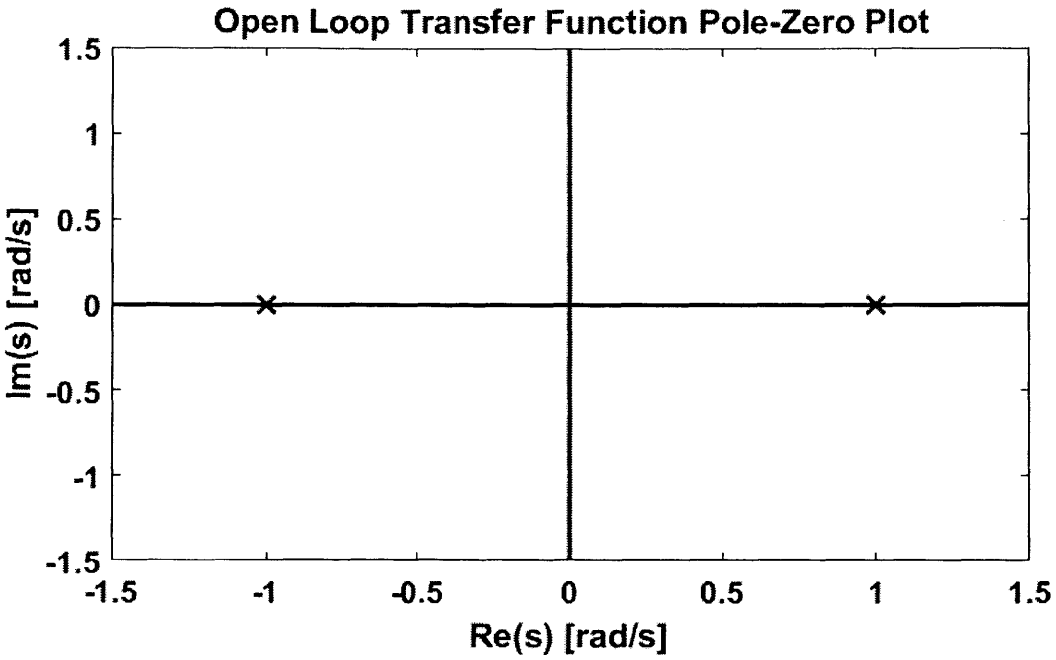

Figure 27: The pole zero plot of the open loop transfer function.

The bode plot of the open loop transfer function is shown in Figure 28. Since the phase never increases above the 180 degree line, the phase margin is zero degrees regardless of the crossover frequency which indicates poor stability. This lack of stability is confirmed by Nyquist analysis.

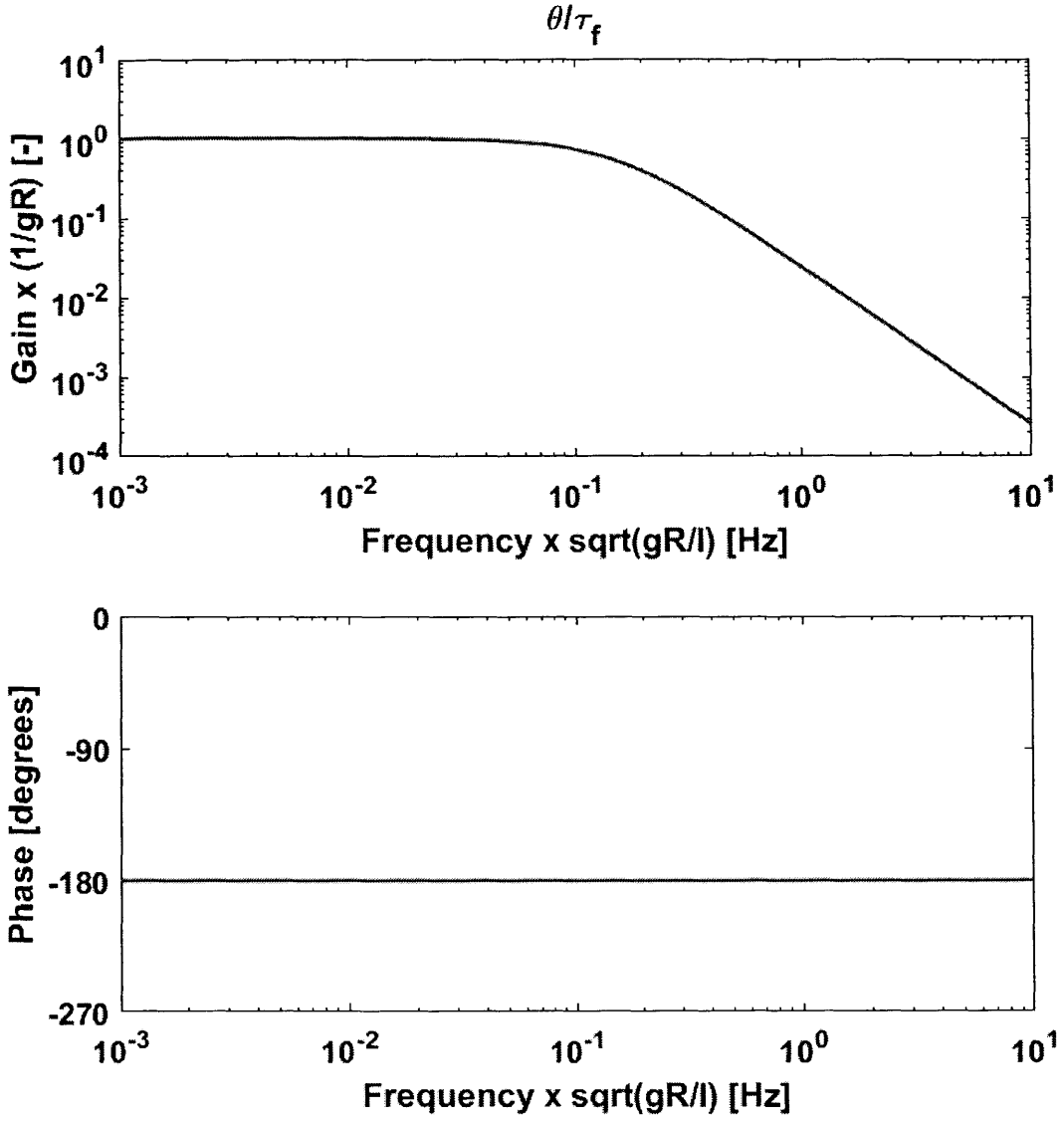

Figure 28: The bode plot of the open loop linear transfer function for the linearized inverted pendulum.

Unfortunately, the full controller design and implementation could not be completed within the scope of this project.

4. Conclusion

In this project the design of a self-balancing monopedal robot was studied. This robot is capable of jumping twice its own body height and is capable of balancing itself in an upright position using reaction wheels. The final leg design was a pantograph linkage driven by a single motor. Analysis on the final parameters of the fabricated robot met or exceeded initial design specifications of jump height and lean angle. Hardware testing will occur as part of future work.

An analysis of the project timeline was conducted using the initial Gantt chart as a baseline. In the course of this project, the scope had to be decreased eliminating the design and fabrication of the testing rig. In addition, implementation and testing of the control system was not completed. The design of the system which was initially scheduled to occur over a period of a week and a half took roughly eight weeks. Generating a refined design when starting from a blank slate proved much more challenging than expected. Elements of the design, in particular the frame were iterated upon heavily as the design became progressively more defined and detailed. Part of the way through the design process the key parameters which drive the design were identified which greatly improved the focus of the design. Since the design used as many off the shelf components as possible along with waterjet and 3D printed components which required minimal post processing, fabrication was completed within the week and a half period which was initially scheduled. Due to delays in other areas the writing process was compressed into less than one week which is significantly shorter than the two and half weeks which were initially scheduled. The high degree of autonomy with this project allowed the design process to be explored as well as the aspects of the technical design as discussed in the rest of the paper. Reflecting on the progression of this project from an engineering management perspective

proved very insightful. Although a fully operating and tested system was not produced, the progress which was achieved by the completion of the design and fabrication of a robust mechanical design in which skills from a wide variety of mechanical disciplines were integrated into a single system made this project a powerful learning experience and a personal success.

Bibliography

Ackerman, Evan. "Salto-1P Is the Most Amazing Jumping Robot We'Ve Ever Seen." IEEE Spectrum, IEEE Spectrum, 29 June 2017, spectrum.ieee.org/automaton/robotics/robotics-hardware/salto1p-is-the-most-amazing-jumping-robot-weve-ever-seen.

Arikawa, Keisuke, and Tsutomu Mita. "Design of Multi-DOF Jumping Robot." IEEE Conference Publication, Wiley-IEEE Press, May 2002, ieeexplore.ieee.org/document/1014358/.

Bosworth, Will, et al. "The MIT Super Mini Cheetah: A Small, Low-Cost Quadrupedal Robot for Dynamic Locomotion." IEEE Xplore, Wiley-IEEE Press, 2012, ieeexplore.ieee.org/abstract/document/7443018/.

Fu, Xin, et al. "Design of a Saltatorial Leg for Jumping Mini Robot." Springer Link, Springer Link, 2010, link.springer.com/chapter/10.1007/978-3-642-16584-9_46.

Geng, Tao, et al. "A Novel One-Legged Robot: Cyclic Gait Inspired by a Jumping Frog." IEEE Conference Publication, Wiley-IEEE Press, 6 Aug. 2002, ieeexplore.ieee.org/xpl/articleDetails.jsp?arnumber=973480&punumber=7658.

Ho, Thanhtam, and Sangyoon Lee. "Design of an SMA-Actuated Jumping Robot." IEEE Xplore, IEEE, 19 July 2010, ieeexplore.ieee.org/document/5513129/.

Kennealy, Gavin, et al. "Design Principles for a Family of Direct Drive Legged Robots." UPenn Scholarly Commons, UPenn Libraries, 3 May 2016, repository.upenn.edu/ese_papers/705/.

Li, Fei, et al. "Jumping like an Insect: Design and Dynamic Optimization of a Jumping Mini Robot Based on Bio-Mimetic Inspiration." Science Direct, Elsevier, 30 Jan. 2012, www.sciencedirect.com/science/article/abs/pii/S0957415812000025.

Wang, Albert, and Sangbae Kim. "Practical Network Based Approach for Computing Safety in Dynamic Systems." MIT, 2018.

Wensing, Patrick M., et al. "Proprioceptive Actuator Design in the MIT Cheetah: Impact Mitigation and High-Bandwidth Physical Interaction for Dynamic Legged Robots." IEEE, Wiley-IEEE Press, June 2017, ieeexplore.ieee.org/abstract/document/7827048/.

Zhang, Jun, et al. "A Bio-Inspired Jumping Robot: Modeling, Simulation, Design, and Experimental Results." *Science Direct*, Elsevier, 12 Oct. 2013, www.sciencedirect.com/science/article/pii/S0957415813001645.

Zheng, Yili, et al. "Mechanical Design and Dynamics Analysis on a Jumping Robot." *Advanced Materials Research*, Trans Tech Publications, 27 Feb. 2012, www.scientific.net/AMR.476-478.1112.

Zuo, Guoyu, et al. "BJR: A Bipedal Jumping Robot Using Double-Acting Pneumatic Cylinders and Torsion Springs." IEEE Xplore, Wiley-IEEE Press, Aug. 2010, ieeexplore.ieee.org/document/5985845/.